

# The Spectral Element Method: An Efficient Tool to Simulate the Seismic Response of 2D and 3D Geological Structures

by Dimitri Komatitsch and Jean-Pierre Vilotte

**Abstract** We present the spectral element method to simulate elastic-wave propagation in realistic geological structures involving complicated free-surface topography and material interfaces for two- and three-dimensional geometries. The spectral element method introduced here is a high-order variational method for the spatial approximation of elastic-wave equations. The mass matrix is diagonal by construction in this method, which drastically reduces the computational cost and allows an efficient parallel implementation. Absorbing boundary conditions are introduced in variational form to simulate unbounded physical domains. The time discretization is based on an energy-momentum conserving scheme that can be put into a classical explicit-implicit predictor/multi-corrector format. Long-term energy conservation and stability properties are illustrated as well as the efficiency of the absorbing conditions. The associated Courant condition behaves as  $\Delta t_C < O(n_{el}^{-1/n_d} N^{-2})$ , with  $n_{el}$  the number of elements,  $n_d$  the spatial dimension, and  $N$  the polynomial order. In practice, a spatial sampling of approximately 5 points per wavelength is found to be very accurate when working with a polynomial degree of  $N = 8$ . The accuracy of the method is shown by comparing the spectral element solution to analytical solutions of the classical two-dimensional (2D) problems of Lamb and Garvin. The flexibility of the method is then illustrated by studying more realistic 2D models involving realistic geometries and complex free-boundary conditions. Very accurate modeling of Rayleigh-wave propagation, surface diffraction, and Rayleigh-to-body-wave mode conversion associated with the free-surface curvature are obtained at low computational cost. The method is shown to provide an efficient tool to study the diffraction of elastic waves by three-dimensional (3D) surface topographies and the associated local effects on strong ground motion. Complex amplification patterns, both in space and time, are shown to occur even for a gentle hill topography. Extension to a heterogeneous hill structure is considered. The efficient implementation on parallel distributed memory architectures will allow to perform real-time visualization and interactive physical investigations of 3D amplification phenomena for seismic risk assessment.

## Introduction

The use of elastic-wave equations to model the seismic response of heterogeneous geophysical media with topography and internal interfaces is a subject that has been intensively investigated by seismologists. The challenge is to develop high-performance methods that are capable of solving the elastic-wave equations accurately and that allow one to deal with large and complicated computational domains as encountered in realistic 3D applications.

This article describes a practical spectral element method to solve the 2D and 3D elastic-wave propagation in complex geometry. The method, which stems from a weak variational formulation, allows a flexible treatment of boundaries, or interfaces, and deals with free-surface boundary conditions naturally. It combines the geometrical flexi-

bility of a low-order method with the exponential convergence rate associated with spectral techniques and suffers from minimal numerical dispersion and diffusion.

Two types of problems have motivated this study. One is elastic waveform modeling, in order to understand and extract quantitative information from complex seismic data. Realistic geological media that present complicated wave phenomena require methods providing solutions of high accuracy that correctly simulate boundary conditions, surface topography, and irregular interfaces with nonhomogeneous properties. The other problem is related to the assessment of site effects in earthquake ground motion. In particular, 3D surface topography, local velocity variations, and layering can produce complicated amplification patterns and energy

scattering. Such effects can modify the ground shaking to a large extent and are relevant for the seismic design of structures.

The need of new high-performance methods for the elastic-wave propagation can be simply assessed when looking back to the continuous efforts that have been devoted to this subject.

Finite-difference methods have been widely implemented with a varying degree of sophistication. Unfortunately, conventional schemes suffer from “grid dispersion,” near large gradient of the wave field, or when too-coarse computational grids are used. For realistic applications (Frankel, 1993; Olsen and Archuleta, 1996; Pitarka and Irigura, 1996), balancing of the trade-off between numerical dispersion and computational cost turns out to be rather difficult. For classical second-order centered finite-difference methods, at least 15 points must be used for the wavelength corresponding to the upper half-power frequency (Kelly *et al.*, 1976; Alford *et al.*, 1974). Grid dispersion and anisotropy can be reduced when using the staggered-grid formulation (Madariaga, 1976; Virieux, 1986; Levander, 1988), which is based on the symmetric first-order hyperbolic form of linear elastodynamics (Hughes and Marsden, 1978). This can also be achieved by using fourth-order centered schemes both in space and time, based on modified wave-equation techniques (Dablain, 1986; Bayliss *et al.*, 1986). Another difficulty with finite differences is their inability to implement free-surface conditions with the same accuracy as in the interior regions of the model and their lack of geometrical flexibility. Even though some techniques have incorporated surface topographies using methods based on grid deformation or vacuum-to-solid taper (Boore, 1972; Jih *et al.*, 1988; Robertsson, 1996; Ohminato and Chouet, 1997) combined with the staggered grid formulation, they often remain limited to simple geometrical transformations and may affect the stability criterion in the case of grid-deformation techniques, or they require up to 15 grid points per shortest wavelength in the case of vacuum-to-solid techniques, which puts some limitations for narrow free-surface structures. All these ripples make finite-difference methods difficult to use for simulating Rayleigh and interface waves in practical situations.

Although more suited to heterogeneous media with complicated geometries, finite-element methods, based on a variational formulation of the wave equations that allows a natural treatment of free-boundary conditions, have attracted somewhat less interest among seismologists (Lysmer and Drake, 1972; Toshinawa and Ohmachi, 1992). Apparently, the main reason for that is that low-order finite-element methods exhibit poor dispersion properties (Marfurt, 1984), while higher-order classical finite elements raise some troublesome problems like the occurrence of spurious waves. Recently, space-time finite-element methods based on Hamilton’s principle, or on time-discontinuous Galerkin formulation, have been introduced for elastodynamics (Hulbert and Hughes, 1990; Richter, 1994).

Alternatively, numerical solutions to the wave equation have been sought via techniques based on integral representations of the problem relating quantities on the physical boundaries. Integral formulations make use of fundamental solutions as weighting functions together with Green’s theorem (Manolis and Beskos, 1988; Bonnet, 1995). In seismology, these methods can be traced back to the pioneering work of Aki and Larner (1970) who used a discrete superposition of plane waves. They have since been extended by many authors (Bouchon, 1979; Sánchez-Sesma and Rosenblueth, 1979; Dravinski and Mossessian, 1987; Horike *et al.*, 1990; Ohori *et al.*, 1992). While direct boundary element methods formulate the problem in terms of the unknown tractions and displacements (Zhang and Chopra, 1991), indirect methods make use of a formulation in terms of force and moment boundary densities (Sánchez-Sesma and Campillo, 1993). The combination of discrete wavenumber expansions for Green’s functions (Bouchon and Aki, 1977; Bouchon, 1979), either with indirect boundary integral representations (Campillo and Bouchon, 1985; Gaffet and Bouchon, 1989) or with direct methods (Kawase and Aki, 1989; Kim and Papageorgiou, 1993), has led to successful methods with the advantage of seeking solutions over a domain one dimension lower than the original form of the problem, with sources at the boundary (removing the uncertainty about their location), and an *a priori* satisfaction of the radiation condition. On the other hand, methods of this kind are most often limited to linear and homogeneous problems and are known to encounter difficulties, such as possible nonuniqueness of the solution of the continuous boundary integral equations at characteristic wavenumbers of the corresponding interior problems, leading to ill-conditioned discrete equations if left uncorrected. Moreover, the resulting linear systems of equations in these methods are very large, nonsymmetric, and dense. The computational advantage in processing time and storage requirements that would be expected intuitively is therefore not always realized in the case of realistic problem sizes.

Spectral methods, introduced in fluid dynamics around 20 years ago by S. A. Orszag, have also been proposed for elastodynamics (Gazdag, 1981; Kosloff and Baysal, 1982). To deal with general boundary conditions, a set of algebraic polynomials (Chebyshev or Legendre in space) replaced the original set of truncated Fourier series. The so-called global pseudo-spectral method (Kosloff *et al.*, 1990) became one of the leading numerical techniques in the 1980s in view of its accuracy, in terms of the minimum number of grid points needed to represent the Nyquist wavelength for non-dispersive propagation. In these methods, numerical solution is derived so as to satisfy the wave equation in differential form at some suitably chosen collocation points. The accuracy is shown to depend strongly on this choice. Unfortunately, global spectral methods suffer from severe limitations: nonuniform spacing of the collocation points for algebraic polynomials puts stringent constraints on the time step that cannot be easily removed (Kosloff and Tal-Ezer,

1993); complicated geometries and heterogeneous material properties cannot be handled easily nor, when the method is based on a strong formulation of the differential equations, realistic free-surface boundary conditions. The use of curvilinear coordinate systems has been proposed to overcome such a limitation (Fornberg, 1988; Tessmer *et al.*, 1992; Carcione and Wang, 1993; Komatitsch *et al.*, 1996) but remains restricted to smooth global mappings of little use for realistic geological models. Another idea is to couple domain decomposition techniques to spectral discretization (Canuto and Funaro, 1988; Carcione, 1991); however, this requires a significant increase of the computational cost.

Understanding of the similarity between collocation methods and variational formulations with consistent quadrature (Gottlieb, 1981; Maday and Quarteroni, 1982) leads in fluid dynamics to the spectral element method (Patera, 1984; Maday and Patera, 1989) that may be related to the  $p$  and  $h - p$  versions of the finite-element methods (Babuška *et al.*, 1981; Babuška and Dorr, 1981). These methods, which bring new flexibility to treat complex geometries, have been proposed for wave propagation recently by Priolo *et al.* (1994) and Faccioli *et al.* (1996).

This article describes a practical spectral element method to solve 2D and 3D elastic-wave propagation in complex geometry. The potentialities of the method are demonstrated on various 2D and 3D problems. In contrast with the method used by Priolo *et al.* (1994), our formulation is based on Legendre polynomials and Gauss-Lobatto Legendre quadrature, leading to fully explicit schemes while retaining the efficient sum-factorization techniques (Orszag, 1980). Although the particular choice of the sets of algebraic polynomials (Chebyshev or Legendre) and collocation points (related to the numerical quadrature) does not generally affect the error estimates significantly, it greatly affects the conditioning and sparsity of the resulting set of algebraic equations and is critical for the efficiency of a parallel iterative procedure (Fisher, 1990).

## Formulation of the Problem

### Initial Boundary-Value Problem

When solutions are assumed to extend to infinity along some directions, a fundamental obstacle to the direct application of numerical methods is the presence of an unbounded domain. The boundary-value problem is therefore converted to a formulation that is defined over a bounded region by introducing an artificial external boundary with appropriate boundary conditions.

We consider an elastic inhomogeneous medium occupying an open, bounded region  $\Omega \subset \mathbb{R}^{n_d}$ , where  $n_d$  is the number of space dimensions (2 or 3 here). The boundary of  $\Omega$  is denoted  $\Gamma$  and can be decomposed into  $\Gamma = \Gamma^{\text{int}} \cup \Gamma^{\text{ext}}$ , where  $\Gamma^{\text{ext}}$  is the artificial external boundary. The displacement and velocity vectors are denoted by  $\mathbf{u}(\mathbf{x}, t)$  and  $\mathbf{v}(\mathbf{x}, t)$ , respectively, where  $\mathbf{x} \in \bar{\Omega}$ , with  $\bar{\Omega}$  the closed region

including physical and external boundaries, and  $t \in \mathbf{I} = [0, T]$ , with  $\mathbf{I}$  the time interval of interest.

For elastic-wave propagation, the equations of motion can be written in compact notation form as

$$\rho \dot{\mathbf{v}} = \text{div} [\boldsymbol{\sigma}] + \mathbf{f}, \quad (1)$$

$$\rho \dot{\mathbf{u}} = \rho \mathbf{v}, \quad (2)$$

with the initial conditions

$$\mathbf{u}(\mathbf{x}, t) = \mathbf{u}_0(\mathbf{x}) \quad (3)$$

and

$$\mathbf{v}(\mathbf{x}, t) = \mathbf{v}_0(\mathbf{x}) \quad (4)$$

on part of the internal boundary  $\Gamma_T^{\text{int}}$ ,

$$\boldsymbol{\sigma}(\mathbf{x}, t) \cdot \mathbf{n}(\mathbf{x}) = \mathbf{T}(\mathbf{x}, t), \quad (5)$$

and on the other part  $\Gamma_g^{\text{int}}$ ,

$$\mathbf{u}(\mathbf{x}, t) = \mathbf{g}(\mathbf{x}, t), \quad (6)$$

where  $\rho = \rho(\mathbf{x})$  is the mass density;  $\mathbf{f}(\mathbf{x}, t)$  is a generalized body force;  $\mathbf{u}_0(\mathbf{x})$  and  $\mathbf{v}_0(\mathbf{x})$  are, respectively, the initial displacement and velocity fields;  $\boldsymbol{\sigma}(\mathbf{x}, t)$  is the stress tensor;  $\mathbf{T}(\mathbf{x}, t)$  is the prescribed boundary traction (Neumann condition); and  $\mathbf{g}(\mathbf{x}, t)$  is the prescribed displacement (Dirichlet condition). A dot over a symbol indicates partial differentiation with respect to time. In component forms,  $\text{div} [\boldsymbol{\sigma}]$  is  $\sigma_{ij,j}$  and  $\boldsymbol{\sigma} \cdot \mathbf{n}$  is  $\sigma_{ij}n_j$ .

Two simple source terms are considered here: a point force,

$$\mathbf{f}(\mathbf{x}, t) = f_i \hat{\mathbf{e}}_i \delta(\mathbf{x} - \mathbf{x}_0) \mathcal{G}(t - t_0), \quad (7)$$

and a body force derived from a seismic moment tensor density distribution,

$$\mathbf{f}(\mathbf{x}, t) = -\text{div} [\mathbf{m}_0(\mathbf{x})] \mathcal{G}(t - t_0), \quad (8)$$

where  $\mathbf{m}_0(\mathbf{x})$  is a symmetric tensor and  $\mathcal{G}(t)$  is a Ricker wavelet in time. The stress is determined by the generalized Hooke's law:

$$\sigma_{ij}(\mathbf{x}) = c_{ijkl}(\mathbf{x}) u_{k,l}(\mathbf{x}, t), \quad (9)$$

where  $u_{k,l} = \partial u_k / \partial x_l$  is the displacement gradient. The elastic coefficients  $c_{ijkl} = c_{ijkl}(\mathbf{x})$  are positive definite and have all the required symmetries. By the minor symmetries  $c_{ijkl} = c_{jikl} = c_{ijlk}$ ,  $\boldsymbol{\sigma}$  depends on the symmetric part of the displacement gradient only.

The representation of the radiation condition associated with the external boundary is a difficult problem, and nu-

merous approximate schemes have been proposed in the geophysical literature, see Bayliss and Turkel (1980) and Givoli (1991) for a review. Exact nonlocal boundary conditions employing an asymptotic expansion of the far-field solution to generate a sequence of local boundary operators (Givoli and Keller, 1990) have now been derived. They are, however, computationally expensive. We assumed here a simple local approximation based on the variational formulation of the paraxial condition originally introduced by Engquist and Majda (1977) and Clayton and Engquist (1977). The local transient impedance of the artificial boundary is approximated by use of a limited wavenumber expansion of the elastodynamics equation in the Fourier domain along the boundary surface. Such an approximation is accurate for high-frequency waves and for waves impinging on the boundary at small angles from the normal direction only. In the following, a first-order approximation, close to the one proposed by Stacey (1988), is retained. On the artificial boundary  $\Gamma^{\text{ext}}$ , the condition is therefore expressed as

$$\mathbf{t} = c_p \rho [\mathbf{v} \cdot \mathbf{n}] \mathbf{n} + c_s \rho \mathbf{v}_T, \quad (10)$$

where  $\mathbf{t}$  is the traction vector on the boundary,  $\mathbf{n}$  is the unit outward normal to the surface,  $\mathbf{v}_T = \mathbf{v} - [\mathbf{v} \cdot \mathbf{n}] \mathbf{n}$  is the projection of the velocity field on the surface, and  $c_p$  and  $c_s$  are the propagation velocities of  $P$  and  $S$  waves, respectively. Such a damping condition was originally proposed by Lysmer and Kuhlemeyer (1969).

### The Variational Form of the Governing Equations

While some methods of approximation directly start from the previous formulation of the initial boundary-value problem (strong form)—the most notable example being the finite difference method—a less restrictive approach consists in considering a weak formulation, or variational formulation, of the original problem that admits a broader range of solutions in terms of regularity or smoothness. The most commonly used formulation is based on the principle of virtual work or virtual displacement (Hughes, 1987; Szabó and Babuška, 1991).

The solution is then searched in the space of the kinematically admissible displacements that is defined, according to the Dirichlet boundary conditions, as

$$\mathcal{S}_t = \{ \mathbf{u}(\mathbf{x}, t) \in H^1(\Omega)^{nd} : \Omega \times \mathbf{I} \rightarrow \mathbb{R}^{nd}; \mathbf{u}(\mathbf{x}, t) = \mathbf{g}(\mathbf{x}, t) \text{ on } \Gamma_g^{\text{int}} \times \mathbf{I} \}, \quad (11)$$

where the subscript  $t$  of  $\mathcal{S}$ , refers to time and  $H^1$  denotes the space of square-integrable functions that possess square-integrable generalized first derivatives.

Introducing the space  $\mathcal{V}$  of the test functions that, in the case of the virtual work formulation, is also called the space of the virtual displacements,

$$\mathcal{V} = \{ \mathbf{w}(\mathbf{x}) \in H^1(\Omega)^{nd} : \Omega \rightarrow \mathbb{R}^{nd}; \mathbf{w}(\mathbf{x}) = \mathbf{0} \text{ on } \Gamma_g^{\text{int}} \}, \quad (12)$$

the weak form of the governing equations can be obtained by multiplying equations (1) through (4) by time-independent test functions  $w$ . Integration by parts and the use of boundary conditions lead to the abstract formulation

$$(\mathbf{w}, \rho \dot{\mathbf{v}}) + a(\mathbf{w}, \mathbf{u}) = (\mathbf{w}, \mathbf{f}) + (\mathbf{w}, \mathbf{T})_{\Gamma_T^{\text{int}}} + (\mathbf{w}, \mathbf{t})_{\Gamma^{\text{ext}}}, \quad (13)$$

$$(\mathbf{w}, \rho \dot{\mathbf{u}}) = (\mathbf{w}, \rho \mathbf{v}), \quad (14)$$

with

$$[\mathbf{w}, \rho \mathbf{u}(\cdot, t)]_{t=0} = (\mathbf{w}, \rho \mathbf{u}_0), \quad (15)$$

$$[\mathbf{w}, \rho \mathbf{v}(\cdot, t)]_{t=0} = (\mathbf{w}, \rho \mathbf{v}_0), \quad (16)$$

where  $a(\cdot, \cdot)$  denotes the bilinear form that expresses the virtual work of the internal stresses, defined as

$$a(\mathbf{w}, \mathbf{u}) = \int_{\Omega} \boldsymbol{\sigma} : \nabla \mathbf{w} \, dV = \int_{\Omega} \nabla \mathbf{w} : \mathbf{c} : \nabla \mathbf{u} \, dV, \quad (17)$$

where in component form  $\boldsymbol{\sigma} : \nabla \mathbf{w} = \sigma_{ij} \partial w_i / \partial x_j$  with the implicit summation convention and  $\mathbf{c}$  is the elastic tensor defined in equation (9).

The bilinear forms  $(\cdot, \cdot)$  can be interpreted as the virtual work of the inertial terms,

$$(\mathbf{w}, \rho \dot{\mathbf{v}}) = \int_{\Omega} \rho \dot{\mathbf{v}} \cdot \mathbf{w} \, dV, \quad (18)$$

and of the external forces,

$$\begin{aligned} (\mathbf{w}, \mathbf{f}) &= \int_{\Omega} \mathbf{f} \cdot \mathbf{w} \, dV; \\ (\mathbf{w}, \mathbf{T})_{\Gamma_T^{\text{int}}} &= \int_{\Gamma_T^{\text{int}}} \mathbf{T} \cdot \mathbf{w} \, d\Gamma; \\ (\mathbf{w}, \mathbf{t})_{\Gamma^{\text{ext}}} &= \int_{\Gamma^{\text{ext}}} \mathbf{t} \cdot \mathbf{w} \, d\Gamma. \end{aligned} \quad (19)$$

### Numerical Discretization

In this section, the Legendre spectral element discretization of the variational statement of the elastic-wave equations is outlined.

Like in a standard finite-element method, the original domain is discretized into  $n_{el}$  nonoverlapping quadrilateral elements:  $\bar{\Omega} = \cup_{e=1}^{n_{el}} \bar{\Omega}_e$ . The restriction of  $\mathbf{w}$  to the element  $\bar{\Omega}_e$  is denoted  $\mathbf{w}^h|_{\bar{\Omega}_e}$ . Each element  $\bar{\Omega}_e$  is mapped onto a reference volume  $\square$  that is defined, in a local  $\xi$  system of coordinates, as a square or a cube  $\Lambda^{nd}$  with  $\Lambda = [-1, 1]$ .

The invertible element mapping  $\mathcal{F}_e$  is defined as:

$\mathcal{F}_e: \square \rightarrow \bar{\Omega}_e$  such that  $\mathbf{x}(\xi) = \mathcal{F}_e(\xi)$ .

With respect to the spatial discretization, we shall require that the variational statement be satisfied for the piecewise-polynomial approximation spaces  $S_N^h \times \mathcal{V}_N^h$ , where  $h$  denotes the characteristic length scale associated with the underlying mesh, defined as

$$S_N^h = \{\mathbf{u}^h \in \mathcal{S} : \mathbf{u}^h \in L^2(\Omega)^{nd} \text{ and } \mathbf{u}^h|_{\bar{\Omega}_e} \circ \mathcal{F}_e \in [\mathbb{P}_N(\square)]^{nd}\} \quad (20)$$

and

$$\mathcal{V}_N^h = \{\mathbf{w}^h \in \mathcal{V} : \mathbf{w}^h \in L^2(\Omega)^{nd} \text{ and } \mathbf{w}^h|_{\bar{\Omega}_e} \circ \mathcal{F}_e \in [\mathbb{P}_N(\square)]^{nd}\}, \quad (21)$$

where  $L^2(\Omega)$  denotes the space of square-integrable functions defined on  $\Omega$  and  $[\mathbb{P}_N(\square)]^{nd}$  denotes the tensor-product space of all polynomials of degree  $N$ , or less, in each of the  $n_d$  spatial directions within the reference volume  $\square$ . The spectral-element spatial discretization can be characterized by the discretization pair  $(n_{el}, N)$ . Each element integral involved in the variational formulation, defined over the domain  $\bar{\Omega}_e$  in the  $\mathbf{x}$  space, is pulled back, using the local mapping  $\mathcal{F}_e$ , on the parent domain  $\square$  and numerically integrated using the numerical quadrature defined as the tensor product of the 1D Gauss–Lobatto Legendre formulas. In order to take advantage of efficient sum-factorization techniques, the  $(N + 1)^{nd}$  basis points for  $\mathbb{P}_N$  are taken to be the same as the quadrature points on each element  $\bar{\Omega}_e$  and define a collocation grid  $\Xi_N^e = \{\xi_i, \eta_j, \zeta_k\}$  that is the  $n_d$ -tensor product of the  $N + 1$  Gauss–Lobatto Legendre integration points.

The piecewise-polynomial approximation  $\mathbf{w}_N^h$  of  $\mathbf{w}$  is defined using the Lagrange interpolation operator  $I_N$  on the Gauss–Lobatto grid  $\Xi_N^e$ :  $I_N(\mathbf{w}|_{\bar{\Omega}_e})$  is the unique polynomial of  $\mathbb{P}_N(\square)$  that coincides with  $\mathbf{w}|_{\bar{\Omega}_e}$  at the  $(N + 1)^{nd}$  points of  $\Xi_N^e$ . If  $l_i^N(\xi)$  denotes the characteristic Lagrange polynomial of degree  $N$  associated with the Gauss–Lobatto point  $i$  of the 1D quadrature formula, the approximation of  $\mathbf{w}|_{\bar{\Omega}_e}$  is defined as

$$\begin{aligned} \mathbf{w}_N^h|_{\bar{\Omega}_e}(x, y, z) &= I_N(\mathbf{w}|_{\bar{\Omega}_e}) \\ &= \sum_{i,j,k=0}^N l_i^N(\xi) l_j^N(\eta) l_k^N(\zeta) w_{ijk}^e, \end{aligned} \quad (22)$$

with  $\mathbf{x} = \mathcal{F}_e(\xi, \eta, \zeta)$  and  $w_{ijk}^e = \mathbf{w}_N^h|_{\bar{\Omega}_e} \circ \mathcal{F}_e(\xi, \eta, \zeta)$ .

A polynomial of degree  $\leq 2N - 1$  can be integrated exactly with  $N + 1$  points. Such a consistent integration, where the quadrature points are the same as the basis points, is shown to be sufficient for complex geometries (Maday and Rønquist, 1990), an important consideration when wave equations are to be solved on significantly deformed geometry or with variable coefficients.

The procedure outlined above leads, like in the finite-

element method, to a coupled system of ordinary differential equations:

$$\mathbf{M}\dot{\mathbf{v}}_t = \mathbf{F}_t^{\text{ext}} - \mathbf{F}_t^{\text{int}}(\mathbf{u}_t, \mathbf{v}_t). \quad (23)$$

Let  $n_{\text{node}}$  be the total number of nodes of the global integration grid  $\Xi_N$  defined as the assembly of the element domain integration grids  $\Xi_N = \cup_e \Xi_N^e$ ; then  $\mathbf{u}_t$  and  $\mathbf{v}_t$  denote the  $n_{\text{node}}$  displacement and velocity vectors, respectively, at a given time  $t$ ;  $\mathbf{F}^{\text{int}}$  is the internal nodal force vector; and  $\mathbf{F}^{\text{ext}}$  is the external forcing vector that includes the source term and the radiation conditions. An attractive property of the method is that, due to the consistent integration scheme and the use of Gauss–Lobatto Legendre formulas, the mass matrix  $\mathbf{M}$  is by construction always diagonal.

The spectral-element method therefore combines the geometric flexibility of the finite-element method with the fast convergence associated with spectral techniques. Considering only spatial errors, an exponential convergence can be ensured (Bernardi and Maday, 1992) for the spectral-element approximation when  $n_{el}$  is fixed and  $N \rightarrow \infty$ . Such a superconvergence derives from the good stability and approximation properties of the polynomial spaces and from the accuracy associated with the Gauss–Lobatto Legendre quadrature and interpolation. The discrete solution suffers from minimal numerical dispersion and diffusion, a fact of primary importance in the solution of realistic geophysical problems, see Tordjman (1995) and Komatitsch (1997) for more details.

The semi-discrete momentum equation is then enforced in conservative form at  $t_{n+a}$ , using two parameters  $\beta$  and  $\gamma$  (Simo *et al.*, 1992):

$$\frac{1}{\Delta t} \mathbf{M} [\mathbf{v}_{n+1} - \mathbf{v}_n] = \mathbf{F}_{n+a}^{\text{ext}} - \mathbf{F}^{\text{int}}(\mathbf{u}_{n+a}, \mathbf{v}_{n+a}), \quad (24)$$

$$\begin{aligned} \mathbf{u}_{n+1} &= \mathbf{u}_n + \Delta t \left[ \left(1 - \frac{\beta}{\gamma}\right) \mathbf{v}_n + \frac{\beta}{\gamma} \mathbf{v}_{n+1} \right] \\ &\quad + \Delta t^2 \left( \frac{1}{2} - \frac{\beta}{\gamma} \right) \mathbf{a}_n, \end{aligned} \quad (25)$$

$$\mathbf{a}_{n+1} = \frac{1}{\gamma \Delta t} [\mathbf{v}_{n+1} - \mathbf{v}_n] + \left(1 - \frac{1}{\gamma}\right) \mathbf{a}_n, \quad (26)$$

where  $\mathbf{u}_{n+a} \doteq \alpha \mathbf{u}_{n+1} + (1 - \alpha) \mathbf{u}_n$  and  $\mathbf{F}_{n+a}^{\text{ext}} \doteq \alpha \mathbf{F}_{n+1}^{\text{ext}} + (1 - \alpha) \mathbf{F}_n^{\text{ext}}$ . Noteworthy properties of this algorithm are exact conservation of the total angular momentum for  $\alpha = \beta/\gamma = 1/2$  (these values define an acceleration-independent time-marching algorithm) and second-order accuracy if and only if  $\alpha = 1/2$ ; for  $\alpha = \beta/\gamma = 1/2$ , a linear analysis shows that the spurious root at zero sampling frequency vanishes if and only if  $\gamma = 1$  (Simo *et al.*, 1992). This Newmark-type scheme can be generalized to a predictor–multi-corrector format (see Appendix B) that improves its properties and allows an efficient parallelization.

**Numerical Implementation.** In the simulations presented in this article, the parameters of the predictor–multi-corrector algorithm are  $\alpha = 1/2$ ,  $\beta = 1/2$ , and  $\gamma = 1$ . The Courant number can be defined as  $n_C = \max [c\Delta t/\Delta x]$ , where  $c$  is the compressional wave speed and  $\Delta x$  is the collocation grid spacing. The associated Courant condition can be shown to behave as  $\Delta t_C < O(n_{ei}^{-1/nd} N^{-2})$ .

The method is shown to work accurately with a low number of grid points per minimum wavelength, corresponding to the upper power frequency  $f_{\max}$  defined in practice as the frequency above which the spectral amplitude of the source becomes less than 5% of the maximum value associated with the fundamental frequency  $f_0$ . For a Ricker wavelet in time, one gets the simple relation  $f_{\max} \approx 2.5 f_0$ . In practice, a spatial sampling of approximately 5 points per minimum wavelength has been found very accurate when working with a polynomial degree of order  $N = 8$ . Below this value, the solution quickly develops significant numerical oscillations during the propagation. Such an abrupt transition is characteristic of methods with minimal numerical dispersion and diffusion.

Typically, for 2D simulations with a 100,000-point curvilinear grid, the memory occupation is of the order of 30 Megabytes, and the CPU time, for a simulation over 2000 time steps, is of the order of 15 min on an Ultra Sparc 1 (140 MHz). For large 3D simulations in a heterogeneous medium, using a 5,000,000-point curvilinear grid, the memory occupation is of the order of 1.5 Gigabyte, and the CPU time, for a simulation over 2000 time steps, is of the order of 1.5 hr on the CM5 128 nodes of the French Centre National de Calcul Parallèle en Sciences de la Terre. In the 3D case, the memory occupation on the CM5 can be higher when using the CMSSL optimized library, which clearly favors CPU efficiency to the detriment of the memory optimization. For details concerning the parallel implementation of the method, we refer to Fisher (1989), Komatitsch (1997), and Komatitsch *et al.* (1997).

## Numerical Examples

### Lamb's Problem

Lamb's problem (Lamb, 1904) is a classical test. The solution can be regarded as the superposition of three main events, the direct  $P$  wave, the direct  $S$  wave, and the Rayleigh wave. When the source is located exactly at the free surface, the main event is the propagation of a strong Rayleigh wave along the surface, which is nondispersive when the medium is homogeneous and the surface is flat.

Lamb's problem is a challenging test for the accuracy of the numerical approximation of the free-surface boundary condition and for the capability of the method to simulate Rayleigh waves correctly. A detailed numerical analysis of this problem can be found in Khun (1985). For the numerical simulation, the free surface has been tilted and the direction of the point force kept normal to it. For this type of mesh,

the Jacobian matrix becomes nondiagonal, allowing, even for small geometrical distortion, one to check the full accuracy of the method and the numerical integration. The analytical solution (see Pilant, 1979) is calculated using the Cagniard–de Hoop technique (de Hoop, 1960) and convolved numerically with the source-time function.

The physical problem is a homogeneous elastic half-space with a  $P$ -wave velocity of  $3200 \text{ m} \cdot \text{sec}^{-1}$ , an  $S$ -wave velocity of  $1847.5 \text{ m} \cdot \text{sec}^{-1}$ , and a mass density of  $2200 \text{ kg} \cdot \text{m}^{-3}$ . The numerical model has a width of 4000 m and a height of 2000 m on the left border. The free surface is tilted by  $10^\circ$ , and the source is located exactly on the free surface, at  $x_s = 1720 \text{ m}$  (see Fig. 1). Absorbing boundaries are used on the left, right, and bottom edges of the model. The mesh is composed of  $50 \times 30$  spectral elements, with a polynomial degree of 8 used in each direction, leading to a total of 96,641 points. The line of receivers goes from  $x = 600 \text{ m}$  to  $x = 3400 \text{ m}$  at the free surface. The variation in time of the point-force source is a Ricker wavelet with a central frequency of 14.5 Hz. The spatial resolution is of the order of 5 points per minimum wavelength. In order to compare to the analytical solution, a rather restrictive time step has been used,  $\Delta t = 0.25 \text{ m sec}$ , which corresponds to  $n_C = 0.25$  for this mesh, approximately 40% of the critical Courant number that is determined empirically to be  $n_C^{\max} = 0.60$ . The total number of time steps is 6000.

A typical snapshot of this simulation (Fig. 1) shows a strong Rayleigh wave with the expected elliptical polarization and a clear head wave. A very good agreement with the exact solution, at receiver 75 located in  $(x, z) = (2695, 2475) \text{ m}$  and at receiver 100 located in  $(x, z) = (3400, 2600) \text{ m}$ , is found, with a maximum error of the order of less than 1%, as shown in Figure 2, where the true amplitudes (without normalization) and the residuals (with a magnification of 10) between the numerical and analytical solutions are plotted. It can also be checked in this figure that the amplitude of the Rayleigh wave does not decay when it propagates along the slope, as expected (Garvin, 1956) in plane strain formulation.

### Garvin's Problem

The second validation example is Garvin's problem (Garvin, 1956), which involves another type of source than in Lamb's problem, for example, a line moment-tensor density that produces a purely explosive source. For a homogeneous elastic half-space, and a source inside the medium, the main events are a direct  $P$  wave, a reflected  $P$  wave, and a  $P$ -to- $S$  mode conversion at the free surface.

The model used, the frequency of the source, and all the numerical parameters are the same as in Lamb's test, except that the explosive source is now located inside the model at  $(x, z) = (2236, 1396.5) \text{ m}$ . Comparison with the analytical solution, at receiver 55 located in  $(x, z) = (2307, 2018.5) \text{ m}$  and at receiver 80 located in  $(x, z) = (3014.5, 2123) \text{ m}$ , is very good with an error that remains less than 1%, as can be seen in Figure 3, where the true amplitudes, as well as

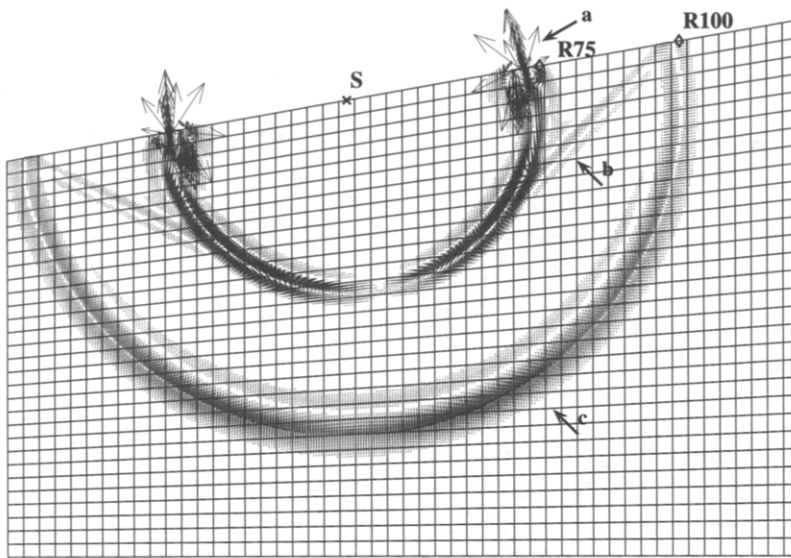


Figure 1. Snapshot showing wave propagation in tilted Lamb's problem. The line-force source is located exactly at the free surface. The cross indicates the source position, and the diamonds represent the position of the receivers. The displacement vector field is displayed. The main event (arrow a) is a strong nondispersive Rayleigh wave that propagates along the free surface with an elliptical polarization. The head wave is shown by arrow b and the direct  $P$  wave by arrow c.

the residuals between the analytical and numerical solutions, are plotted as in Figure 2. Numerical errors are limited to small spurious reflections at the absorbing boundaries.

#### Energy-Momentum Conservation and Stability of the Absorbing Conditions

To assess some of the properties of the time-marching algorithm, the propagation of elastic waves in a rectangular homogeneous domain, with the same elastic properties as in Lamb's test, has been simulated.

The four sides of the model are first assigned to be free surfaces, and an explosive source is prescribed within the model. The time step used in this experiment is  $\Delta t = 0.40$  m sec, corresponding to a Courant number of 0.30, 50% of the maximal Courant number  $n_C^{\max}$ . The time-marching algorithm is the predictor–multi-corrector scheme of Appendix B, with  $\alpha = 1/2$ ,  $\beta = 1/2$ , and  $\gamma = 1$ . The qualitative features of the dynamics of the system are displayed in Figure 4. The long-term stability is apparent from these results. After  $10^5$  time steps, the total energy is perfectly conserved without oscillations, and correct conversions between kinetic and potential energy are observed.

Using the same model, but now enforcing first-order radiation conditions on the four sides, the efficiency of the absorbing boundary conditions can be assessed. For exact absorbing boundaries, the total energy is expected to decay monotonically to zero as the spherical waves propagate outside the domain. The total energy during the simulation is shown in Figure 5 to decay as expected with no oscillations. A small residual energy, typically of the order of  $10^{-4}$  of the total energy of the source, remains in the medium and is related to spurious reflected waves of small displacement amplitude (a few percents of the amplitude of the outgoing waves) produced by the low-order-absorbing boundary conditions. The spurious reflections are themselves rapidly absorbed, and the energy finally drops to zero.

## Two-Dimensional Numerical Simulations

More realistic 2D simulations are now considered to illustrate the ability of the method to take into account surface topography, deformed interfaces, and complex boundary conditions.

### Free-Surface and Interface Topography

A layered elastic half-space with a prescribed topography is considered. The upper layer is characterized by a  $P$ -wave velocity of  $2000 \text{ m} \cdot \text{sec}^{-1}$ , an  $S$ -wave velocity of  $1300 \text{ m} \cdot \text{sec}^{-1}$ , and a mass density of  $1000 \text{ kg} \cdot \text{m}^{-3}$ . The lower-layer elastic parameters are a  $P$ -wave velocity of  $2800 \text{ m} \cdot \text{sec}^{-1}$ , an  $S$ -wave velocity of  $1473 \text{ m} \cdot \text{sec}^{-1}$ , and a mass density of  $1500 \text{ kg} \cdot \text{m}^{-3}$ . A strong contrast both in velocity and in Poisson's ratio is hence modeled, with  $\nu = 0.13$  for the lower layer and  $\nu = 0.38$  for the upper layer. The source is explosive and located inside the upper layer, just below the free surface, so as to excite a strong Rayleigh wave along the curved topography.

The numerical model has a width of 2500 m and an average height of 1700 m. The line of receivers goes from  $x = 700$  m to  $x = 2100$  m at  $z = 1380$  m. The source position is  $(x, z) = (620, 1853)$  m. The mesh is composed of  $48 \times 40$  elements, with a polynomial approximation of order  $N = 8$ , and a total number of collocation grid points of 123,585. The explosive source is a Ricker wavelet in time, with a central frequency of 15 Hz. The number of points per minimal wavelength is of the order of 5. The time step is  $\Delta t = 0.30$  m sec, which corresponds to a Courant number of 0.45, 70% of the maximal Courant number  $n_C^{\max}$ . The simulation is done over 5000 time steps.

A typical snapshot of the simulation is shown in Figure 6, and the seismograms recorded by the receivers are shown in Figure 7. A strong Rayleigh wave can be observed prop-

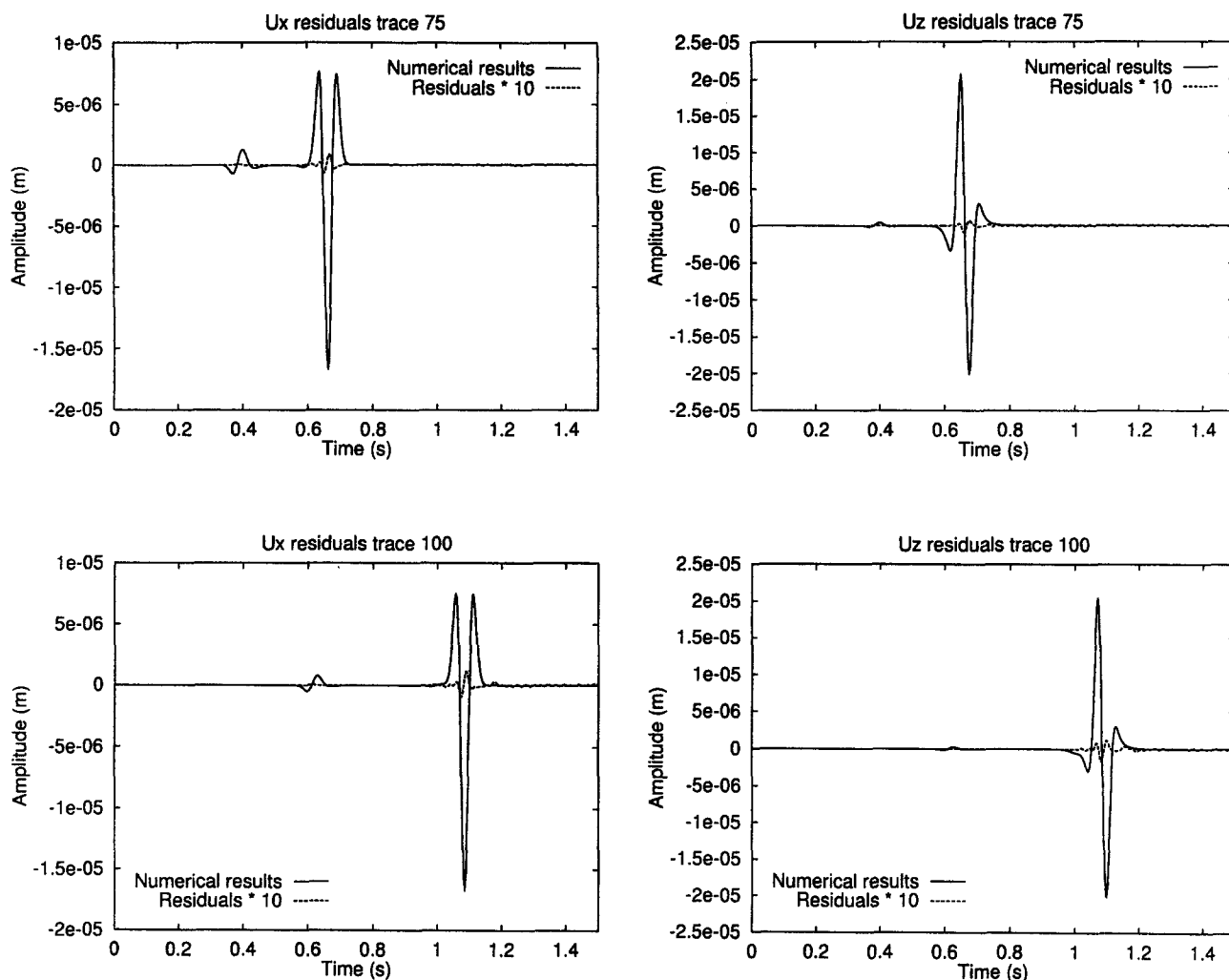


Figure 2. Time evolution of the horizontal and vertical components of the displacement at receivers 75 and 100, along the free surface, for tilted Lamb's problem with a line-force source as in Figure 1. The amplitude of the Rayleigh wave remains constant along the free surface, as expected for plane strain. The residuals with respect to the analytical solution are also displayed, with an amplification factor of 10, on the same plot. A very good agreement is found, and a minimal dispersion is observed. The maximum relative error remains less than 1%.

agating along the topography, with a Rayleigh-to-body-wave mode conversion, particularly clear on the snapshot after the  $S$  wave converted at the free surface, when the Rayleigh wave encounters a change of curvature at the free surface. Such a mode conversion is in agreement with the theoretical study of Rulf (1969) and previous numerical studies by Jih *et al.* (1988) and Komatitsch *et al.* (1996).

The second model includes a real topography derived from a structure in the Peruvian Andes (courtesy of Elf Aquitaine) as shown in Figure 8 with no vertical exaggeration. We consider a simple homogeneous elastic half-space. The elastic parameters are a  $P$ -wave velocity of  $3200 \text{ m} \cdot \text{sec}^{-1}$ , an  $S$ -wave velocity of  $1848 \text{ m} \cdot \text{sec}^{-1}$ , and a mass density of  $2200 \text{ kg} \cdot \text{m}^{-3}$ . The explosive source is located near the free surface inside the model.

The numerical model has a width of 5500 m, and the

mean height of the topography is of the order of 1300 m. The source position is  $(x, z) = (1000, 670) \text{ m}$ . The mesh is composed of  $60 \times 12$  elements, with a polynomial approximation of order  $N = 8$  and a total number of collocation points of 46,657. The explosive source is a Ricker wavelet in time, with a central frequency of 12 Hz. The number of points per minimal wavelength is of the order of 5. The time step is  $\Delta t = 0.30 \text{ m sec}$ , which corresponds to  $n_C = 0.45$ . The number of time steps in this simulation is 5000. The line of receivers is placed at the surface between  $x = 900 \text{ m}$  and  $x = 5000 \text{ m}$ .

A typical snapshot of the simulation is shown in Figure 8, and the recorded seismograms are shown in Figure 9. For a flat free surface, the seismograms should be characterized by a single arrival. As expected for a foothill zone, topographical effects are of major importance and induce, in par-

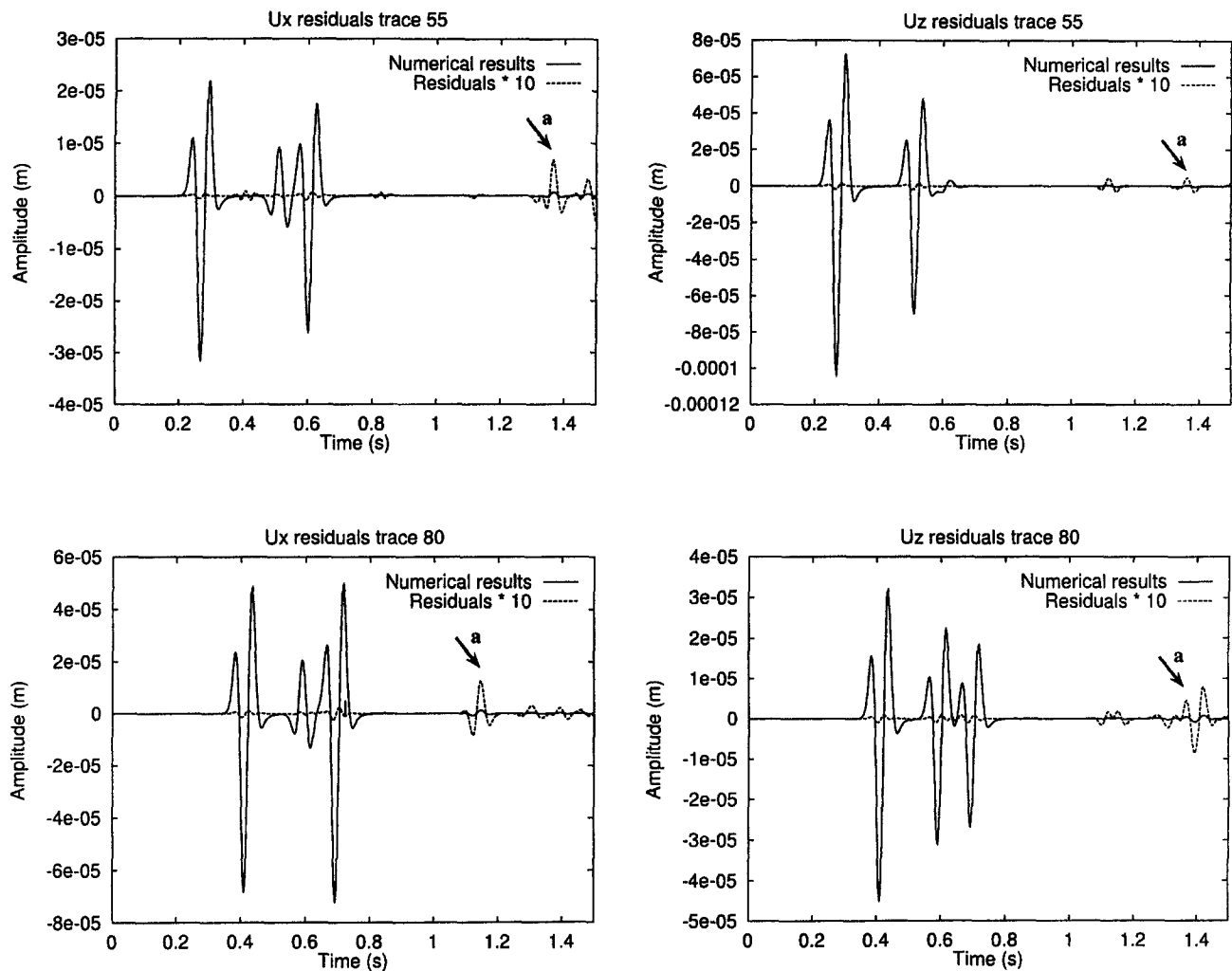


Figure 3. Time evolution of the horizontal and vertical components of the displacement at receivers 55 and 80 for tilted Garvin's problem with a compressive volumetric source. The residuals with respect to the analytical solution are also displayed, with an amplification factor of 10, on the same plot. A very good agreement is observed, and the maximum error remains less than 1%. A small spurious reflection from the absorbing boundaries can be observed and is indicated by arrow a.

ticular, some strong diffracted phases and conversions from Rayleigh to body waves.

#### Step at the Free Surface

The problem considered is the transmission and reflection of a Rayleigh wave at a step of the free surface, for example, the so-called "corner problem," and can be related, for instance, to a cliff or a fault at the free surface (see, for example, Lapwood, 1961; Hudson and Knopoff, 1964; de Breaecker, 1958). This problem is very sensitive to the accuracy of the free-surface boundary condition, and *ad hoc* numerical treatments of the free-surface boundary condition at the corner are sometimes introduced that may perturb the relative amplitudes of the different phases.

The physical problem is a homogeneous elastic quarter-space. The source is a line force located just below the upper

free surface. The elastic parameters are a  $P$ -wave velocity of  $3200 \text{ m} \cdot \text{sec}^{-1}$ , an  $S$ -wave velocity of  $1847.5 \text{ m} \cdot \text{sec}^{-1}$ , and a mass density of  $2200 \text{ kg} \cdot \text{m}^{-3}$ . The numerical model has a width of  $4000 \text{ m}$  and a height of  $2400 \text{ m}$ . To simulate a quarter-space, absorbing boundaries are used on the left and bottom sides of the mesh. The source position is  $(x, z) = (2440, 2340) \text{ m}$ . The normal and tangential components of the displacement are recorded by a line of receivers placed around the corner on the free surface, between  $(x, z) = (2600, 2400) \text{ m}$  and  $(x, z) = (4000, 1000) \text{ m}$ . The mesh is composed of  $50 \times 30$  elements, with a polynomial approximation of order  $N = 8$ . The total number of collocation points is  $96,641$ . The line-force source is a Ricker wavelet in time with a central frequency of  $14.5 \text{ Hz}$ . The number of points per minimum wavelength is of the order of 5. The time step is  $\Delta t = 0.50 \text{ m sec}$ , and the simulation is done

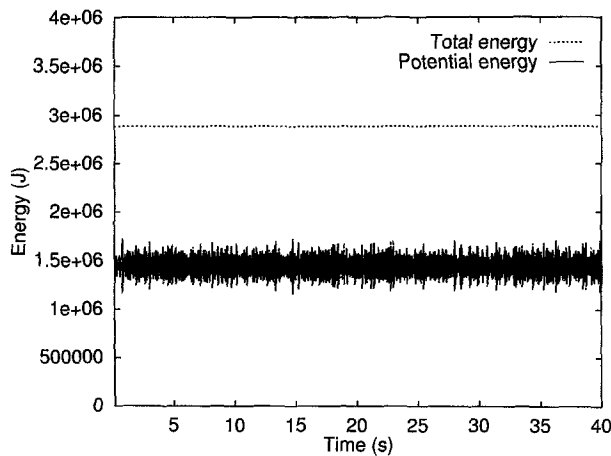


Figure 4. Long-term stability of the energy-momentum conserving time scheme for the case of a homogeneous elastic medium, bounded by free-surface boundaries, with an explosive source inside the volume. The time evolution of the total and potential energy is displayed for  $10^5$  time steps and a step size of  $\Delta t = 0.40$  m sec. The total energy is shown to remain constant during the simulation.

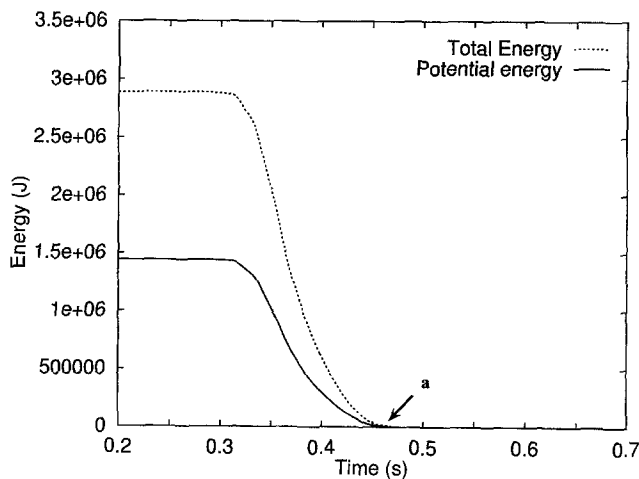


Figure 5. Energy evolution for the case of a homogeneous medium, all bounded by absorbing boundaries, with an explosive source. The total energy decreases rapidly as the energy is radiated outside the domain. Small spurious reflections may appear for waves impinging on the sides at small incidence due to the zeroth-order approximation used here. These spurious reflections, that keep a small fraction of the total energy in the system (less than a few percent), disappear as soon as they reach a new absorbing boundary. This effect is hardly visible on this figure due to the scale and can only be observed when zooming the area indicated by arrow a.

over 5000 time steps. The normal and tangential components of the displacement are recorded by the receivers on both surfaces.

The time response of the displacement is shown in Figure 10. A strong Rayleigh wave propagating along the upper side is observed. This Rayleigh wave is partly reflected and partly transmitted at the corner. The transmitted Rayleigh wave can be seen traveling down the right side of the model, and the corner acts as a diffraction point, triggering spherical  $P$  and  $S$  waves and small Rayleigh waves.

### Three-Dimensional Numerical Simulations

To illustrate the capabilities of the spectral element method for 3D problems, a simple parametric study of the diffraction of elastic waves by a local surface topography has been carried out. This study is motivated by the recent results of Bouchon *et al.* (1996) and Bouchon and Barker (1996) on the effects of a small 3D hill and their implication for strong ground motion, as, for example, the strong accelerations, of the order of 1.82  $g$ , recently recorded on top of the Tarzana hill during the 1994 Northridge, California, earthquake (Spudich *et al.*, 1996).

Surface topography has long been recognized as responsible for energy diffraction and scattering effects that are associated with the observations of late arrivals, mostly Rayleigh waves [see, for example, the early study of Gilbert and Knopoff (1960)], and these effects are considered today as an important source of seismic coda (Clouser and Langston, 1995). Numerous field experiments, performed on hills and mountain ridges, have also shown that surface topography can induce strong amplifications and variations of the ground motion during earthquakes as a result of subsurface focusing and scattering of the radiated energy (Umeda *et al.*, 1986; Carver *et al.*, 1990; Sánchez-Sesma, 1997). Recently, these effects were evidenced by the well-instrumented dramatic examples of the 1994 Northridge, California, earthquake (Spudich *et al.*, 1996; Gao *et al.*, 1996) and the 1995 Kobe, Japan, earthquake (Toki *et al.*, 1995; Iwata *et al.*, 1996), both with epicenters inside urban areas.

Although the need to include the influence of local site topography in seismic risk assessment and microzonation studies is now well recognized (Bard, 1982; Gaffet and Bouchon, 1989; Sánchez-Sesma and Campillo, 1993; Pedersen *et al.*, 1994), the calculated levels of amplification are very often underestimated. Besides possible effects due to the nonlinear behavior of soils, or variations in shear-wave velocity, comparisons of the observations of Spudich *et al.* (1996) with theoretical and numerical results indicate that the three dimensionality of the topography and its internal structure are important factors. In the case of Tarzana hill, transverse oscillations of the 3D elongated structure were found to be of major importance (Spudich *et al.*, 1996; Bouchon and Barker, 1996), both in the observations and in the simulations. Surprisingly, very few theoretical investigations

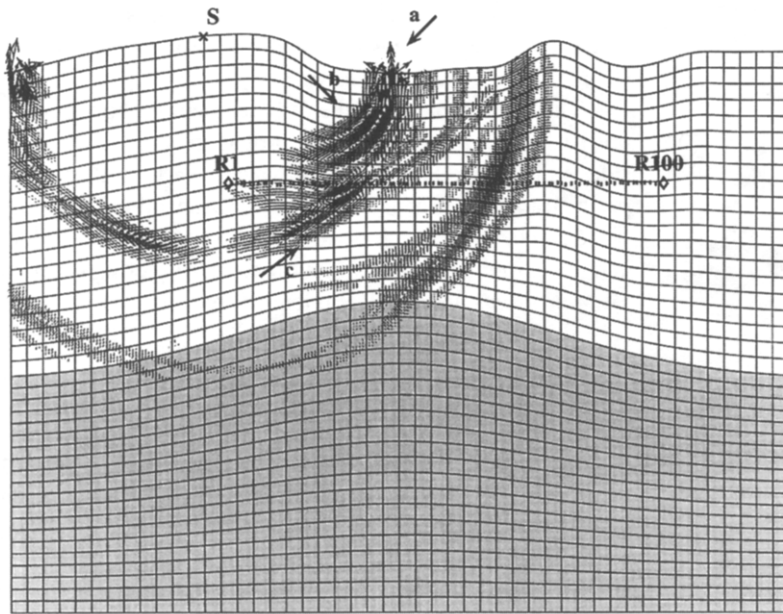


Figure 6. Snapshot showing wave propagation in the case of a layered elastic half-space with curved free surface and interface. The source is explosive and is located within the volume just below the free surface as indicated by the cross. The dotted line represents the position of the receivers. Displayed is the displacement vector field. A Rayleigh wave that propagates along the topography is observed (arrow a), with a strong Rayleigh-to-body-wave mode conversion (arrow b) just after the converted S wave at the free surface (arrow c), that occurs when the Rayleigh wave encounters a change of curvature along the free surface.

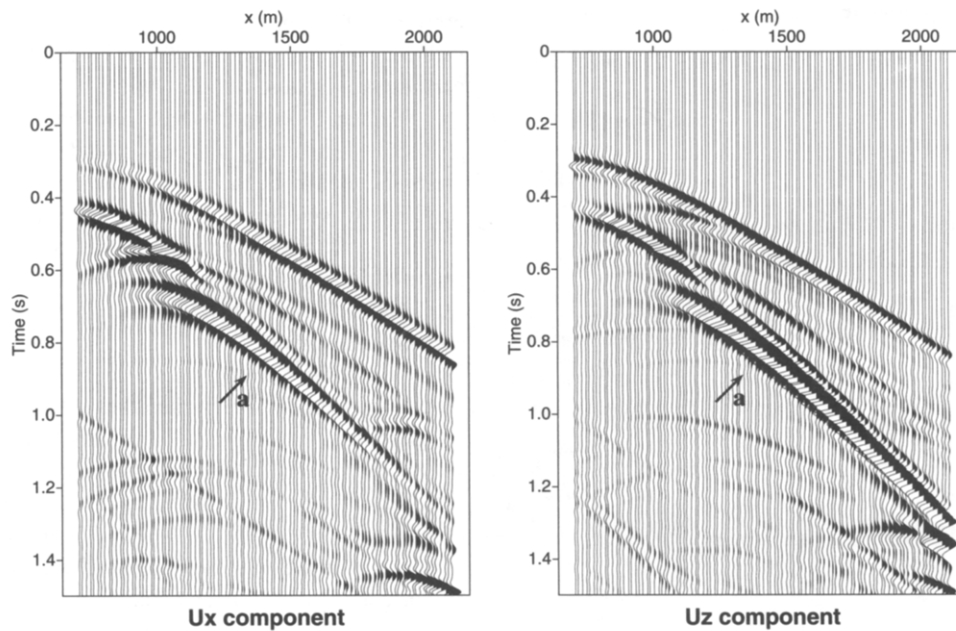


Figure 7. Time responses of the horizontal and vertical components of the displacement, at the receivers placed inside the model, in the case of the layered elastic half-space of Figure 6. The strong later event (arrow a), traveling with an S-wave velocity, corresponds to a Rayleigh-to-body-wave mode conversion when the Rayleigh wave encounters a strong change of curvature along the free surface. Arrivals at around  $t = 1.2$  sec are reflections from the curved interface, with also some spurious reflections from the absorbing boundaries.

of 3D surface irregularities have been reported (Sánchez-Sesma, 1983; Sánchez-Sesma and Luzón, 1996; Bouchon *et al.*, 1996; Bouchon and Barker, 1996).

In the following, the spectral-element method is shown to be an effective tool for investigating the diffraction of elastic waves by 3D structures, in the case of both a homogeneous and a stratified medium.

#### Amplification by a Three-Dimensional Hill

Following Bouchon *et al.* (1996), the topography is a gentle 3D hill and is simply parameterized by

$$z(x, y) = z_0 + h_0 \exp\left(-\frac{(x-x_0)^2}{2\sigma_x^2}\right) \exp\left(-\frac{(y-y_0)^2}{2\sigma_y^2}\right), \quad (27)$$

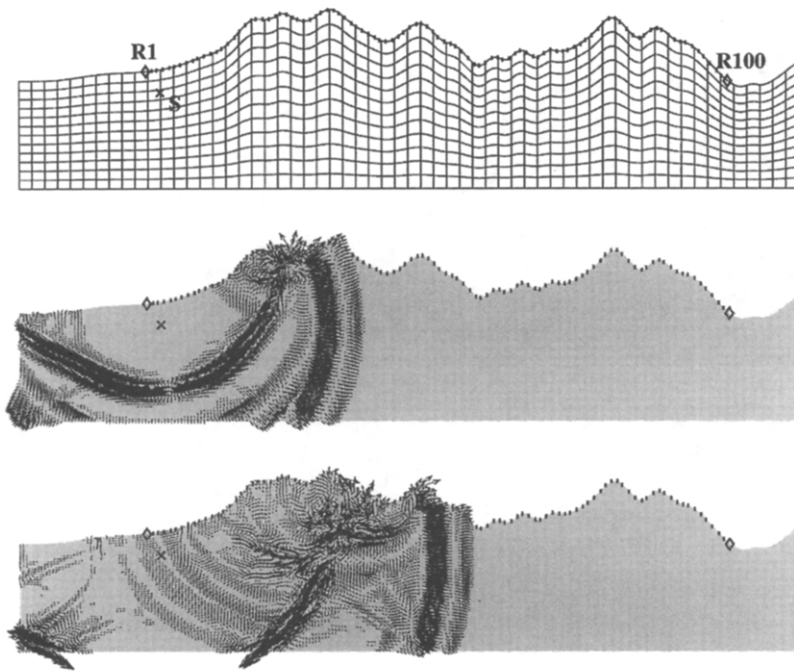


Figure 8. Snapshots showing wave propagation for a homogeneous elastic section across the Peruvian Andes (courtesy Elf-Aquitaine). Displayed are the displacement vector field and the real topography with no vertical exaggeration. The length of the section is 5500 m, and the average height of the topography is of the order of 1300 m. The dotted line represents the position of the receivers, and the source position is indicated by a cross. Even for such a simple homogeneous model, the effect of the strong topography is very important, with diffracted phases that are superimposed to the direct wave. Rayleigh-to-body-wave conversions can also be seen.

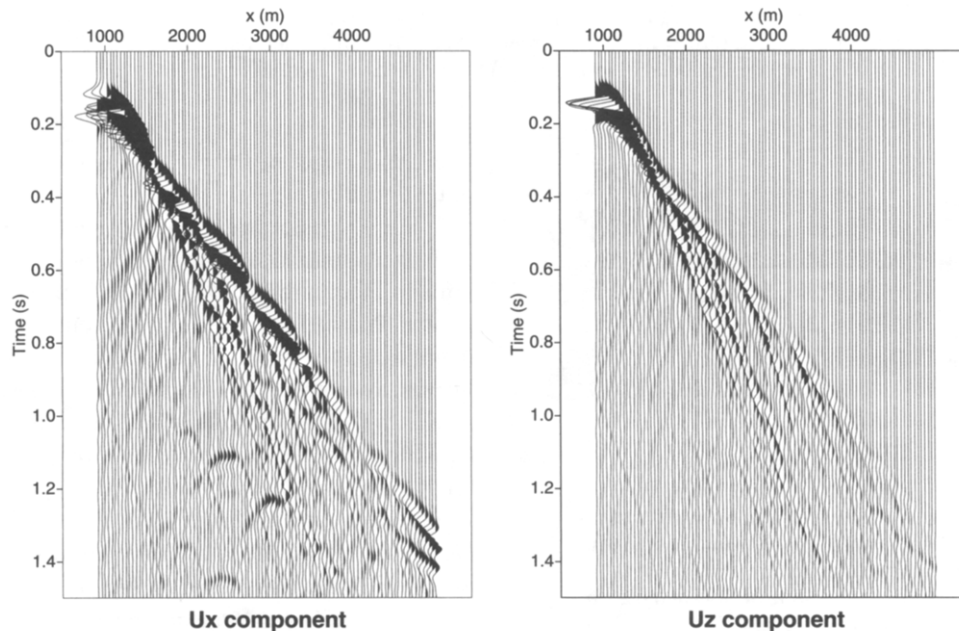


Figure 9. Time responses of the horizontal and vertical components of the displacement at the receivers placed along the free surface in the case of the Peruvian cross section of Figure 8. The section is supposed to be elastic and homogeneous. Diffraction from the strong topography is particularly clear on both components. Without topography, only a single arrival would be observed.

with  $z_0 = 1050$  m,  $x_0 = 1040$  m,  $y_0 = 1040$  m,  $\sigma_x = 250$  m,  $\sigma_y = 125$  m, and  $h_0 = 180$  m. The size of the model is  $2080 \times 2080 \times 1050$  m, and the mesh is composed of  $26 \times 26 \times 14$  elements, with a polynomial order of  $N = 8$ , corresponding to a total number of points of 4,935,953 (see Fig. 11a).

*Case of a Homogeneous Medium.* A homogeneous elastic medium is first considered, as in Bouchon *et al.* (1996), with a  $P$ -wave velocity of  $3200 \text{ m} \cdot \text{sec}^{-1}$ , an  $S$ -wave velocity of  $1847.5 \text{ m} \cdot \text{sec}^{-1}$ , and a density of  $2200 \text{ kg} \cdot \text{m}^{-3}$ . The structure is excited by a vertically incident plane  $S$  wave that is polarized along either the minor or the major axis of the

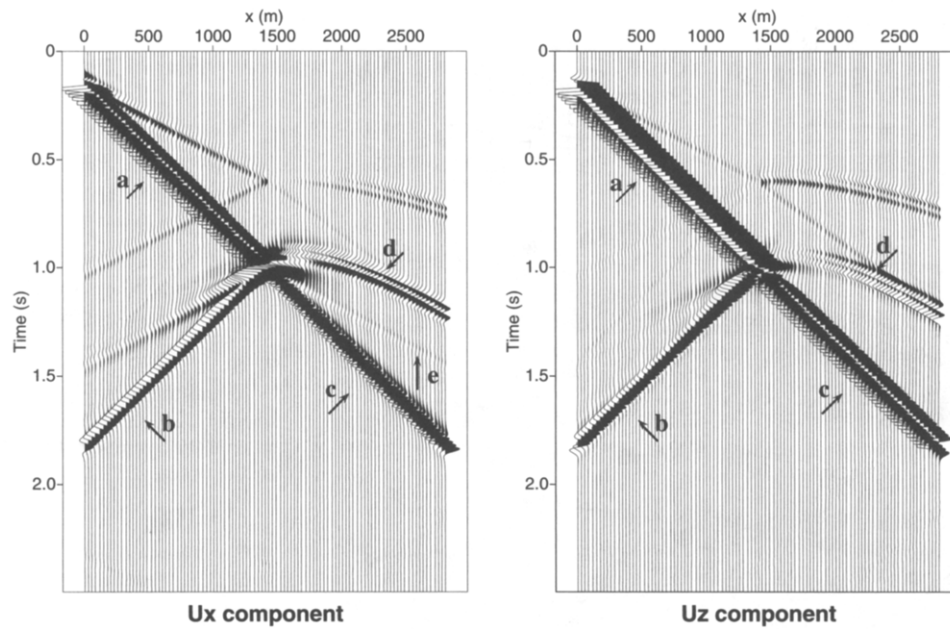


Figure 10. Time responses of the horizontal and vertical components of the displacement vector at the receivers placed around the corner for the model consisting of a step at the free surface. A strong Rayleigh wave propagating along the upper free surface can be observed (arrow a). This surface wave is partly reflected (arrow b) and partly transmitted (arrow c) by the corner that acts as a diffraction point, triggering  $P$  and  $S$  waves (arrows d and e, respectively) with typical diffraction hyperbola.

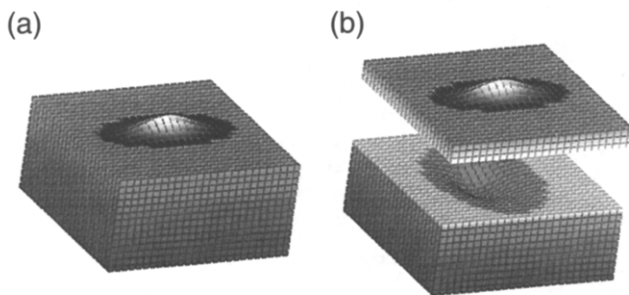


Figure 11. Three-dimensional models: (a) a 3D Gaussian shape topography is considered in the case of an homogeneous elastic half-space and (b) a stratified elastic half-space with a nonsymmetrical basin. The topography is characterized by a height of  $h_0 = 180$  m and a standard deviation of 250 and 125 m along the  $x$  and  $y$  axis, respectively. The size of the model is  $2080 \times 2080 \times 1050$  m. The mesh is composed of  $26 \times 26 \times 14$  elements, with a polynomial order of  $N = 8$  in each direction. The total number of collocation points is 4,935,953.

topography. The source is a Ricker wavelet in time, of maximal amplitude 0.5, and two fundamental wavelengths are investigated:  $\lambda_s = h$  or  $\lambda_s = 3h$ , where  $h$  is the maximum height of the hill. The corresponding fundamental frequencies of the Ricker are  $f_h = 10.2$  Hz and  $f_{3h} = 3.4$  Hz. The simulated timescale spans 0.8 sec, with a time step of  $\Delta t = 0.5$  m sec. Periodic boundary conditions are implemented on

the lateral edges of the grid to simulate a plane wave in an infinite half-space.

For a vertically incident  $S$  wave of wavelength  $\lambda_s = h$  polarized along the minor axis, Figure 12 shows the surface ground motion recorded along the minor axis of the topography. The main features are a strong amplification of the amplitude of motion, on the hill, and very clear diffracted waves, away from the topography, composed of a surface  $P$  wave and a Rayleigh wave. In the vicinity of the hill, the amplitude of the Rayleigh wave is of the same order as that of the surface  $P$  wave, but, as it propagates, the  $P$ -wave amplitude decreases faster, with a  $1/r$  decay for the  $P$  wave versus a  $1/\sqrt{r}$  decay for the Rayleigh wave, and the Rayleigh wave becomes the dominant feature. A strong directivity effect induced by the topography is observed when comparing the time response of the  $y$  component of the displacement recorded along the minor and major axes, as shown in Figure 13: The diffracted surface wave clearly propagates preferentially along the minor axis.

The response of the elastic structure for two vertically incident  $S$  waves with  $\lambda_s = h$  and  $\lambda_s = 3h$ , polarized along the minor or the major axis of the topography, is shown in Figure 14. The time evolution of the horizontal displacement amplitude recorded at the surface is plotted for the two incident wavelengths,  $\lambda_s = h$  and  $\lambda_s = 3h$ , in the case of an incident Ricker wavelet having a maximal amplitude of 0.5. Each frame of these movies is numbered in the upper left corner. This number indicates the time elapsed from the be-

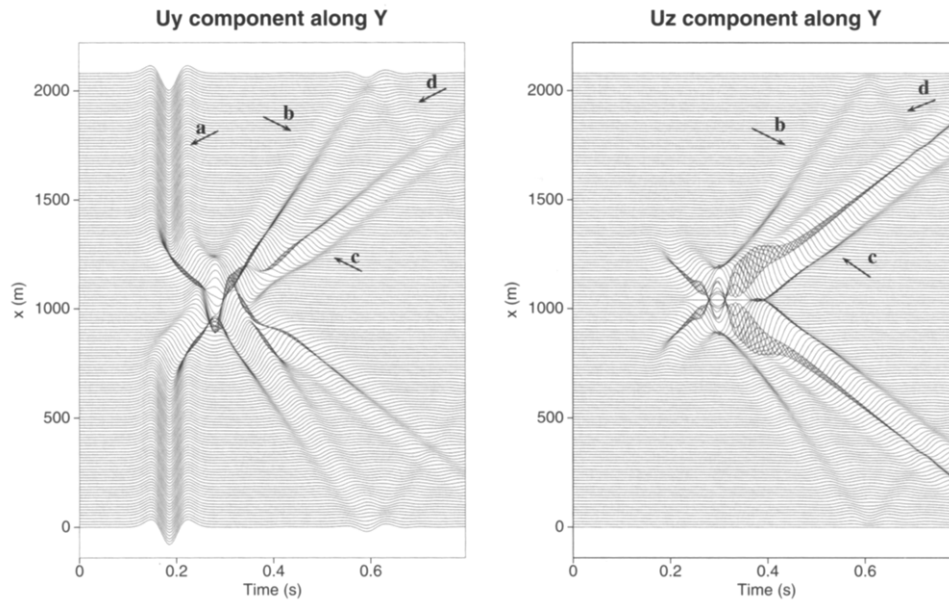


Figure 12. Time responses of the  $y$  (horizontal) and  $z$  (vertical) components of the displacement vector at the receivers placed on the free surface, along the minor axis ( $y$ -direction) of the topography, for the 3D homogeneous model of Figure 11(a) with a vertical incident  $S$  wave of wavelength  $\lambda_s = h$ , polarized along the minor axis. The direct  $S$  wave is clearly seen on the  $y$  horizontal component (arrow a), with two waves diffracted by the topography: a  $1/r$  decaying  $P$  wave (arrow b) and a Rayleigh wave (arrow c). Small artificial phases (arrow d) are observed near the edges of the model due to the lateral periodic boundary conditions used in the simulation.

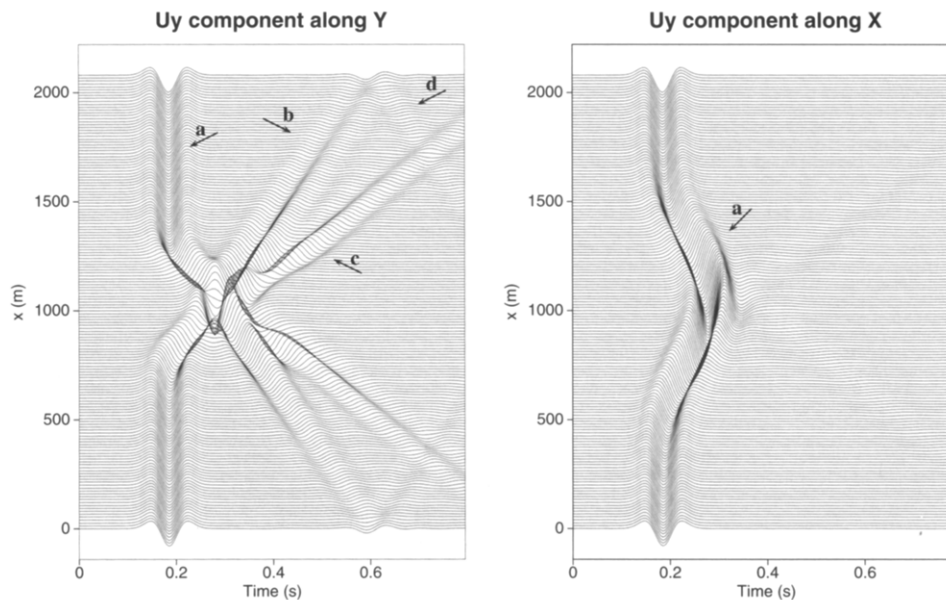


Figure 13. Time responses of the  $y$  (horizontal) component of the displacement vector at the receivers placed on the free surface, along the minor axis ( $y$  direction) and the major axis ( $x$  direction) of the topography for the 3D homogeneous model. The vertical incident  $S$  wave, of wavelength  $\lambda_s = h$ , is polarized along the minor axis. The direct  $S$  wave can be seen on both directions. A strong directivity effect, due to the 3D geometry of the topography, is observed on the diffracted  $P$  (arrow b) and Rayleigh (arrow c) waves that appear mainly on the recordings done along the minor axis.

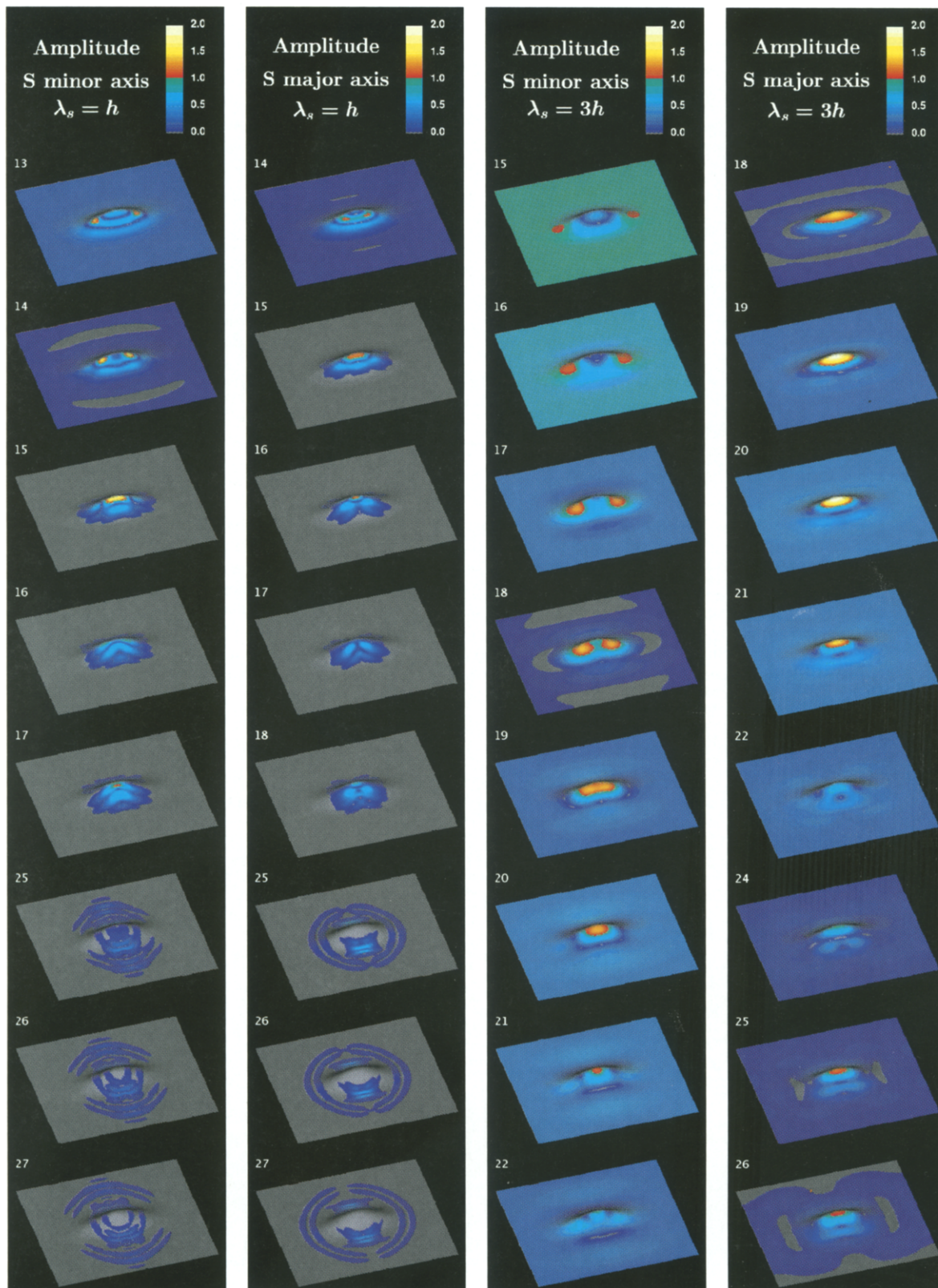


Figure 14. Snapshots showing the amplitude of the horizontal projection of the displacement vector field at the surface for an incident  $S$  wave, with a wavelength  $\lambda_s = h$  or  $\lambda_s = 3h$ , polarized along the minor or the major axis. The slides are numbered in the upper left corner, and the time step between two consecutive numbers is 20 m sec. A strong directivity in the wave propagation along the topography can be observed. The maximum amplification, of the order of two, is observed for the case of an incident wavelength  $\lambda_s = h$  and a polarization along the minor axis.

gining of the simulation, in units of 20 m sec. The first few frames, corresponding to the arrival of the direct wave, have been suppressed.

A strong directivity in the propagation of the diffracted energy can again be observed: The surface wave propagates preferentially along the minor axis of the topography independently of the polarization of the incident wave, while the surface *P* wave propagates in the direction of polarization. The relative amount of diffraction at the top and bottom of the hill is difficult to quantify for these wavelengths, even if most of the diffracted energy appears to be generated at the top of the hill. The maximum amplification is of a factor 2 and is recorded at the summit for  $\lambda_s = h$  and for an incident polarization along the minor axis (frame 15). In this case, the diffracted surface *P* and the Rayleigh waves are generated preferentially along the minor axis (frames 26 and 27). This can be clearly seen on the polarization diagram recorded along the minor axis and the major axis (see Fig. 15). Along the minor axis, besides the direct wave, a Rayleigh

wave with a nice retrograde elliptical polarization is observed as well as a strong diffracted *P* wave with a small polarization effect due to the curvature of the topography. In contrast, along the major axis, a very small, and rapidly attenuating, diffracted *S* wave can be observed. With the same wavelength but incident polarization along the major axis (see Fig. 14), the amplification gets weaker, of the order of 1.2 on frame 15, and while a wave is still propagating at the surface along the minor axis, the diffracted *P* wave now propagates along the major axis (see frames 26 and 27). This can also be analyzed on the polarization diagrams of Figure 16. Along the minor axis, besides the direct wave, no Rayleigh wave can be observed. The diffracted energy is composed of a small body wave that is interpreted as an *S* wave, with an  $1/r$  attenuation, propagating at the surface. Along the major axis, the diffracted energy is mainly a *P* wave. At the summit, a strong amplification is observed with a nice polarization due to the curvature of the topography.

In contrast, for a larger incident wavelength,  $\lambda_s = 3h$ ,

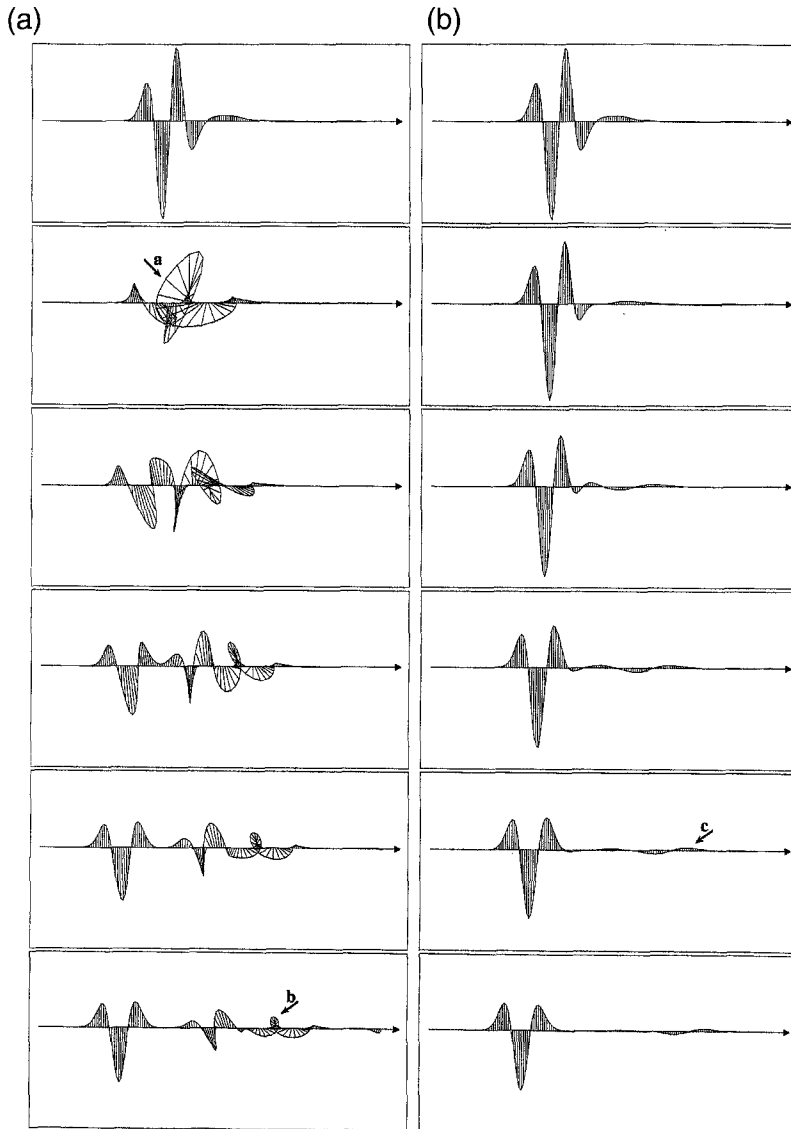


Figure 15. Polarization diagrams at different receivers along (a) the minor axis (*y* direction), and (b) the major axis (*x* direction) of the topography for the 3D homogeneous model and a vertically incident *S* wave, of wavelength  $\lambda_s = h$ , polarized along the minor axis. Displayed is the projection of the displacement vector onto the plane defined by the *y* and *z* directions. The upper display corresponds to a receiver located on top of the topography, while the others are for receivers located at 80, 160, 240, 320, and 400 m from the summit. Along the minor axis, a strong diffraction (arrow *a*) is observed with, besides the direct *S* wave, a clear Rayleigh wave that propagates down the hill with an elliptical polarization (arrow *b*) and a diffracted *P* wave with small polarization due to the curvature effect of the topography. Along the major axis, very small diffracted energy is produced, and only a small surface *S* wave (arrow *c*) can be observed.

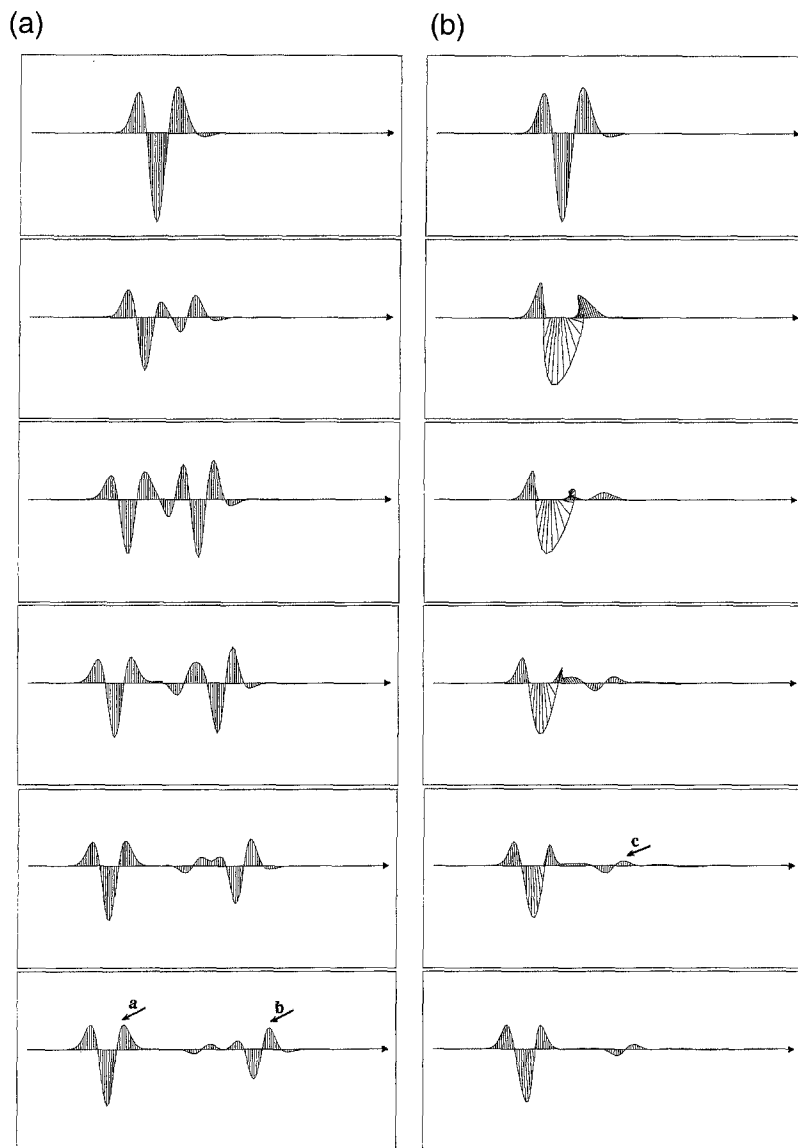


Figure 16. Polarization diagrams at different receivers along (a) the minor axis ( $y$  direction), and (b) the major axis ( $x$  direction) of the topography for the 3D homogeneous model and a vertically incident  $S$  wave, of wavelength  $\lambda_s = h$ , polarized along the major axis. Displayed is the projection of the displacement vector onto the plane defined by the  $x$  and  $z$  directions. The positions of the receivers are the same as in Figure 15. Along the minor axis, besides the direct  $S$  wave (arrow a), no clear diffracted  $P$  wave can now be observed, while a diffracted  $S$  wave (arrow b) still propagates at the surface along that direction in contrast with Figure 15. A diffracted  $P$  wave (arrow c) now propagates along the major axis but is of smaller amplitude than in the case of Figure 15.

a strong amplification, of the order of 1.7, is now observed at the summit for an incident polarization along the major axis (see frame 20 in Fig. 14). For such a large incident wavelength, the diffracted waves are difficult to identify (see frame 26). An interesting breathing phenomena can be observed over a period of 80 m sec between frames 20 and 25, the strong amplification on frame 20 is dimmed (frame 21) and disappears on frames 22 and 24 to reappear on frames 25 and 26. No unique interpretation has yet been obtained. It may be related to an oscillation of the structure, for example, the hill coupled to the elastic half-space, or to a residence time for constructive phase interference of the diffracted waves within the hill structure.

The amplification pattern on the hill exhibits a strong variability. The maximal amplification can occur in a small area around the summit, or at mid-slope, while the summital area is exhibiting a deamplification; see frame 16 for  $\lambda_s = 3h$  with an incident polarization along the minor axis. A given area may be submitted several times to strong ampli-

fication events, like, for example, in the oscillation that appears in the case of  $\lambda_s = 3h$  with a polarization along the major axis.

The transfer function of the structure is shown in Figure 17. It is computed as the ratio between the spectral amplitude of the component of the displacement colinear to the polarization of the incident wave, and the spectral amplitude of the incident wave. In Figure 17, the ratio has been calculated using the results of the simulation with a Ricker wavelet of fundamental wavelength  $\lambda_s = h$ .

For a polarization along the minor axis, a strong amplification is observed at the top of the hill for high frequencies (15 to 30 Hz). At low frequency, the central mode of the structure can be observed, with a resonance effect. For about 5 Hz, two maxima of the amplification are observed at mid-slope, while a strong deamplification occurs at the top of the hill. These two maxima can be associated with a kind of resonance due to the beginning of constructive interferences inside the hill structure. The transfer function along the mi-

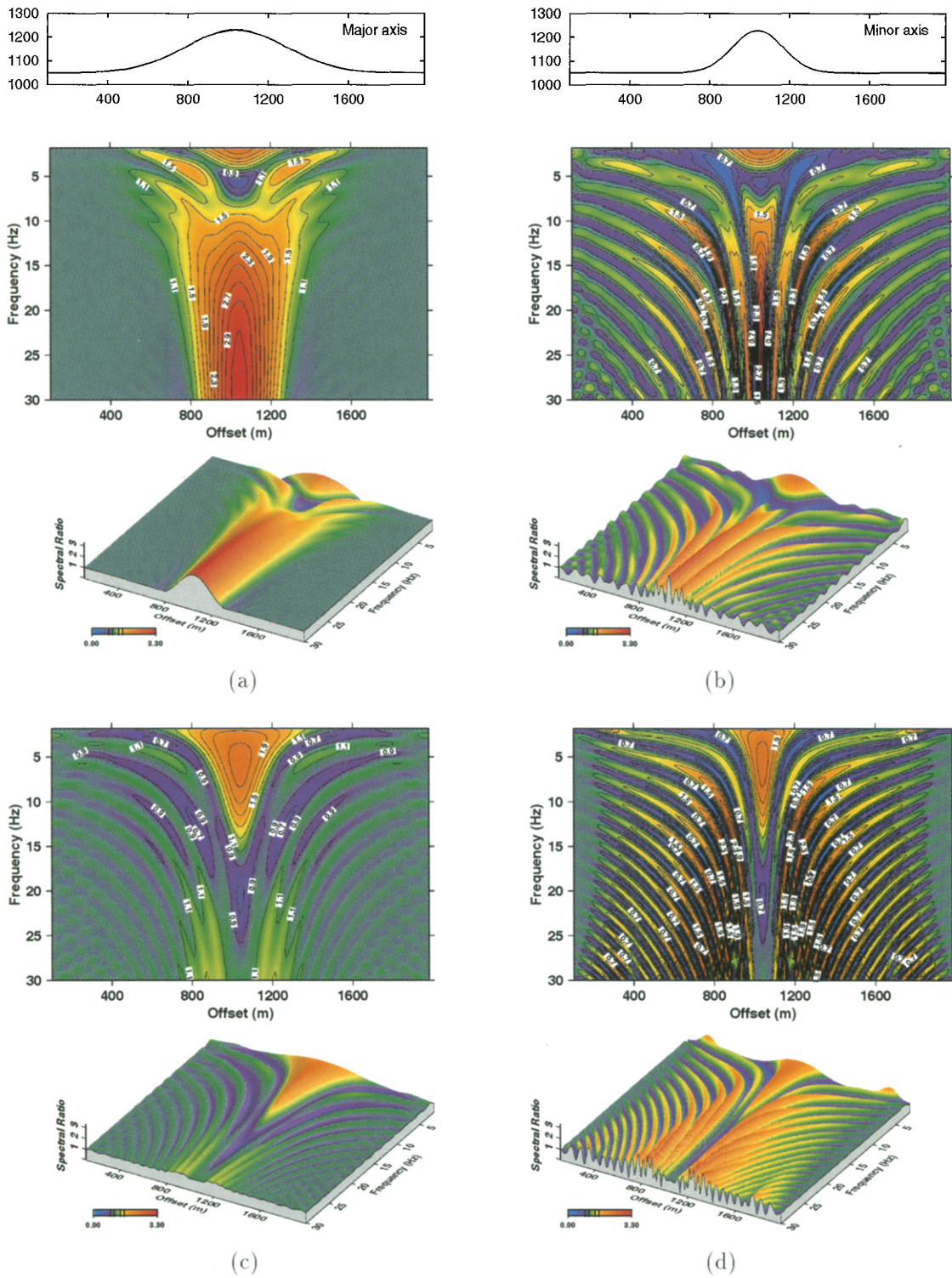


Figure 17. Transfer function for the response of the 3D homogeneous model to a vertically incident  $S$  wave of wavelength  $\lambda_s = h$ : (a) response along the major axis for an incident polarization along the minor axis; (b) response along the minor axis for an incident polarization along the minor axis; (c) response along the major axis for an incident polarization along the major axis; and (d) response along the minor axis for an incident polarization along the major axis. The transfer function is computed as the ratio between the spectral amplitude of the component of the displacement vector along the direction of polarization and the spectral amplitude of the incident wave. A strong amplification pattern can be observed.

nor axis is clearly modulated by the Rayleigh and surface  $P$  waves that travel downward.

For a polarization along the major axis, a broad amplification occurs at the top of the hill for low frequencies, up to 10 Hz, while at higher frequencies (15 to 30 Hz), a small deamplification is now observed. Due to the directivity effect, modulation by the surface wave propagating down the minor axis can be observed, while the modulation along the major axis is now due to the diffracted  $P$ -wave propagation.

The transfer function computed with the results of the simulation done for  $\lambda_s = h$  can be convolved with the source function for  $\lambda_s = 3h$  in order to generate the seismograms along the minor and major axes. Comparison of the synthetic seismograms obtained by convolution to the simulated ones for  $\lambda_s = 3h$  allows one to check the accuracy, or at least the consistency, of the different simulations. The result is shown in Figure 18 for an incident polarization along the minor axis and at two receivers along the minor axis only: on top and at the base of the topography. The agreement is very good and attests the consistency of the method over a wide range of frequencies. The wiggle observed at 0.8 sec on the records is due to the fact that the actual simulated time was exactly 0.8 sec.

*Case of an Asymmetrical Sedimentary Basin in the Presence of Topography.* A two-layer elastic half-space having the same surface topography has also been considered. The

lower layer is characterized by a  $P$ -wave velocity of  $3200 \text{ m} \cdot \text{sec}^{-1}$ , an  $S$ -wave velocity of  $1847.5 \text{ m} \cdot \text{sec}^{-1}$ , and a density of  $2200 \text{ kg} \cdot \text{m}^{-3}$  as before. The upper layer now has a  $P$ -wave velocity of  $2000 \text{ m} \cdot \text{sec}^{-1}$ , an  $S$ -wave velocity of  $1155 \text{ m} \cdot \text{sec}^{-1}$ , and a density of  $1500 \text{ kg} \cdot \text{m}^{-3}$ . The free-surface topography and the dimensions of the model remain the same as in the homogeneous case. The geometry of the lower surface of the sedimentary basin is given by

$$z(x, y) = z_b - h_b \exp\left(-\frac{(x-x_0)^2}{2\sigma_x^2}\right) \exp\left(-\frac{(y-y_0)^2}{2\sigma_y^2}\right), \quad (28)$$

with  $z_b = 825 \text{ m}$ ,  $h_b = 200 \text{ m}$ ,  $x_0 = 900 \text{ m}$ ,  $y_0 = 1040 \text{ m}$ , and  $\sigma_x = 246 \text{ m}$ , if  $x \leq x_0$ ;  $\sigma_x = 237 \text{ m}$ , if  $x > x_0$ ;  $\sigma_y = 320 \text{ m}$ , if  $y \leq y_0$ ; and  $\sigma_y = 246 \text{ m}$ , if  $y > y_0$ . The basin is not centered with respect to the free-surface topography, and the edges of this basin themselves are nonsymmetrical (see Fig. 11b).

Due to the contrast in velocity and Poisson's ratio between the upper and lower layers of the model, this simulation clearly requires more computer resources than in the case of the homogeneous example. In particular, the simulated timescale has to be substantially increased in order to capture the response of the structure. The results presented here are just a preliminary attempt, and extended simulations

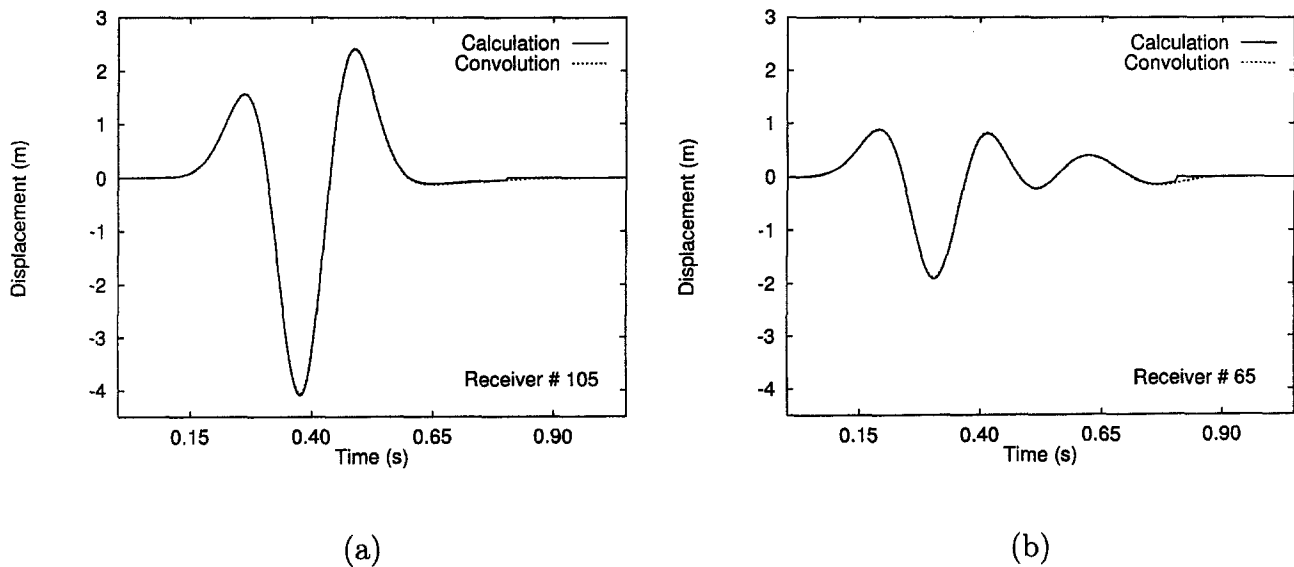


Figure 18. Comparison between the time response of the  $y$  component of the displacement vector, at two receivers, obtained from a direct simulation and from the convolution of the transfer function by the source function of the simulation. The receivers are (a) at the top of the hill and (b) at the base of the hill along the minor axis. The simulation was performed for a vertically incident  $S$  wave polarized along the minor axis with  $\lambda_s = 3h$ . The transfer function is the one of Figure 17a computed from the results of the simulation with an incident wavelength of  $\lambda_s = h$ . A very good agreement is observed up to  $t = 0.8$  sec, which is exactly the time at which the numerical simulation ended.

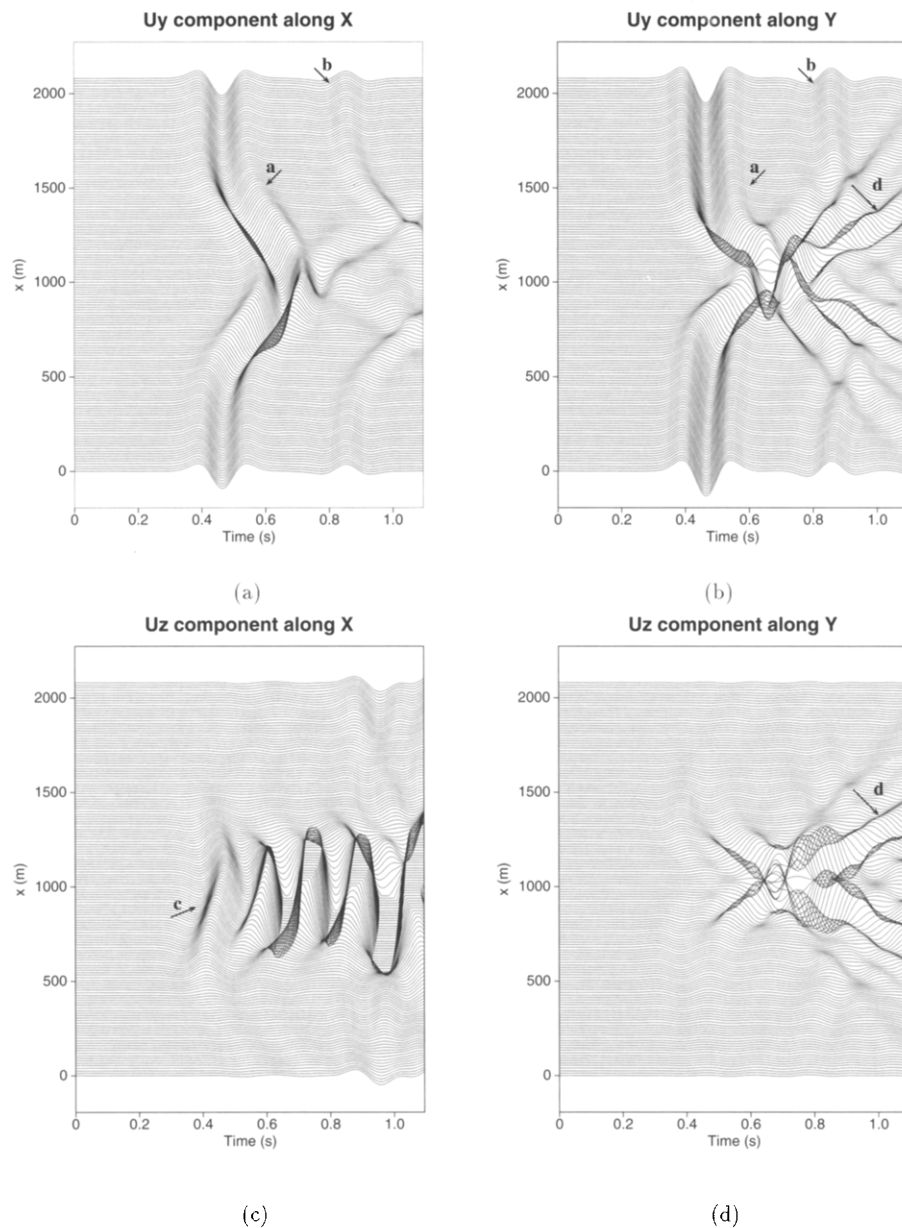


Figure 19. Time responses of the  $y$  (horizontal) and  $z$  (vertical) components of the displacement vector at the receivers placed on the free surface, along the major axis ( $x$  direction) and the minor axis ( $y$  direction) of the topography, for the 3D heterogeneous model of Figure 11a, with a vertically incident  $S$  wave of wavelength  $\lambda_s = 2h$  polarized along the minor axis. The direct  $S$  wave is clearly identified on the  $y$  component of the displacement (arrow a), with a deflection due to the shape of the basin. The first multiple can be observed (arrow b) on the  $y$  component in both directions and produces a distortion of the diffracted Rayleigh (arrow d) and  $P$  waves that is particularly clear along the minor axis. For the vertical  $z$  component of the displacement, the amplitudes along the major axis have been saturated to a third of the maximal amplitude in order to extract the converted  $S$  to  $P$  wave at the bottom of the basin (arrow c). Along the minor axis, the Rayleigh wave has a vertical component that can be clearly seen (arrow d).

are still required. They are, however, interesting enough to illustrate the application of the spectral-element method to realistic 3D structures.

The simulation is performed for an incident plane  $S$  wave of wavelength  $\lambda_s = 2h$ , polarized along the minor axis. The seismograms recorded at the free surface along the mi-

nor and the major axes of the topography are shown in Figure 19.

The main features, for this incident wavelength, are the result of the superposition of two weakly interacting effects: the shape of the surface topography and the shape of the sedimentary basin. The effects of the basin structure remain

limited in this simulation. The study of more complex examples would have required larger models (mainly in terms of computer memory) that were beyond our computer resources.

In Figures 19a and 19b, the distortion of the direct wave due to the structure of the basin can be seen as well as the first multiple, which is quite strong here due to the high reflection coefficient, of the order of 0.4, that has been assumed in this simulation. In particular, in Figure 19b, the distortion of the diffracted  $P$  and Rayleigh waves by the first  $S$ -wave multiple is quite clear. Due to the limited timescale of the simulation, only the first multiple has been simulated. In Figure 19c, the amplitudes have been saturated at about a third of the maximal amplitude in order to extract the converted  $S$  to  $P$  wave at the bottom of the basin that can be seen here as the first arrival. In Figure 19d, the vertical component of a clear Rayleigh wave diffracted by the topography can be observed and must be considered as the complement of the horizontal component observed in Figure 19b, in order to give the classical elliptical polarization. These limited responses already show some of the interesting phenomena produced by the complicated geological structure: smaller Rayleigh-wave velocity in the case of the sedimentary layer, presence of an  $S$ -wave multiple created by reflection at the bottom of the basin, and small  $S$ -to- $P$  mode conversion generated on the edges of the basin. The arrival time and the waveform of the first multiple, created in the sedimentary layer, have been checked and shown to be consistent with the thickness and the velocities of this layer.

## Conclusions

A practical spectral-element method for calculating the propagation of seismic waves through 2D and 3D geological structures has been presented. The method is based on a high-order variational formulation of elastodynamics that allows the natural treatment of an irregular free surface. The procedure proposed in this article is based upon semi-discretization: For the spatial discretization, the spectral-element approximation is used, producing a system of ordinary differential equations in time, which in turn is discretized using a finite-difference method for ordinary differential equations. More specifically, an energy-momentum conserving algorithm in time, which can be put into a classical predictor–multi-corrector format, has been used. The spectral-element method is shown on various examples to combine the geometrical flexibility of a low-order finite-element method with the rapid convergence rate associated with spectral techniques, even when dealing with deformed geometries or heterogeneous elastic properties.

Classical 2D problems, Lamb and Garvin, for which analytical solutions exist, have been studied to assess the accuracy of the method. The discrete solution is shown to present minimal numerical dispersion and diffusion. A high accuracy is obtained using only 5 points per minimal wave-

length. Moreover, long-term energy-conserving and stability properties of the method have been shown.

The capabilities of the method to handle complex free-surface geometries and deformed internal interfaces have been illustrated by solving realistic 2D problems: One involves a step at the free surface, while the other includes a realistic geological topography based on a cross section along the Peruvian Andes. In both cases, Rayleigh waves and complex surface-to-body-wave conversions have been accurately modeled. The method provides a very flexible tool to understand and extract, at low computational cost, quantitative physical information from complicated wave phenomena such as diffraction, conversion, and generation of Rayleigh or interface waves that occur in geophysical applications.

Finally, the spectral method is shown to be an efficient tool for studying the diffraction of elastic waves by 3D surface topographies and its effect on strong ground motion. Complex amplification patterns, in space and time, are shown to occur even for a gentle 3D hill. The results obtained in this study are in very good agreement with those obtained by Bouchon *et al.* (1996) using a boundary integral method. The method allows one to handle a heterogeneous internal structure below the topography, which leads to interesting geophysical applications for seismic risk assessment and microzonation studies.

The method can be efficiently implemented on distributed memory parallel machines. The typical CPU time for an average 2D simulation, using a mesh of the order of 100,000 points, and simulating 2000 time steps, is 4 min on 64 nodes of a CM5. The largest 3D simulation treated in this article involves a  $26 \times 26 \times 14$  elements mesh, with a polynomial approximation order of  $N = 8$ , leading to a 5,000,000-point curvilinear grid. Such a simulation, with 64 bits computation and 2000 time steps, requires 1.5 hr on 128 nodes of a CM5. This will allow real-time visualization and interactive physical analysis of amplification phenomena and seismic risk assessment using modern distributed memory parallel architectures.

## Acknowledgments

The authors are very grateful to F. J. Sánchez-Sesma for numerous discussions of the 3D results and for providing them with Garvin's solution. They would also like to thank Y. Maday and R. Madariaga for fruitful discussions all along this work. Stimulating discussions with G. Seriani and E. Priolo are also acknowledged. Many thanks to C. Caqueneau and P. Stoclet for their help in the implementation of the code on the CM5. G. Moguilly provided an invaluable support for the 3D visualizations. The constructive remarks of the reviewers T. Ohminato and L.-J. Huang are also acknowledged. This work has been partly supported by the French Centre National de Calcul Parallèle en Sciences de la Terre (CNCPTST).

## References

- Aki, K. and K. L. Larner (1970). Surface motion of a layered medium having an irregular interface, due to incident plane  $SH$  waves, *J. Geophys. Res.* **75**, 933–954.

- Alford, R., K. Kelly, and D. Boore (1974). Accuracy of finite difference modeling of the acoustic wave equation, *Geophysics* **39**, 834–842.
- Babuška, I. and M. R. Dorr (1981). Error estimates for the combined  $h$  and  $p$  version of the finite element method, *Numer. Math.* **37**, 257–277.
- Babuška, I., B. A. Szabó, and I. N. Katz (1981). The  $p$  version of the finite element method, *SIAM J. Numer. Anal.* **18**, 512–545.
- Bard, P. Y. (1982). Diffracted waves and displacement field over two dimensional topographies, *Geophys. J. R. Astr. Soc.* **71**, 731–760.
- Bayliss, A. and E. Turkel (1980). Radiation boundary conditions for wave-like equations, *Comm. Pure Appl. Math.* **33**, 707–725.
- Bayliss, A., K. E. Jordan, B. J. LeMesurier, and E. Turkel (1986). A fourth-order accurate finite-difference scheme for the computation of elastic waves, *Bull. Seism. Soc. Am.* **76**, 1115–1132.
- Bernardi, C. and Y. Maday (1992). *Approximations Spectrales de Problèmes aux Limites Elliptiques*, Springer-Verlag, Paris.
- Bonnet, M. (1995). *Équations Intégrales et Éléments de Frontière*, Paris, CNRS Éditions, Eyrolles.
- Boore, D. M. (1972). A note on the effect of simple topography on seismic SH waves, *Bull. Seism. Soc. Am.* **62**, 275–284.
- Bouchon, M. (1979). Discrete wavenumber representation of elastic wave fields in three space dimensions, *J. Geophys. Res.* **84**, 3609–3614.
- Bouchon, M. and K. Aki (1977). Discrete wavenumber representation of seismic-source wave fields, *Bull. Seism. Soc. Am.* **67**, 259–277.
- Bouchon, M. and J. S. Barker (1996). Seismic response of a hill: the example of Tarzana, California, *Bull. Seism. Soc. Am.* **86**, 66–72.
- Bouchon, M., C. A. Schultz, and M. N. Tököz (1996). Effect of three-dimensional topography on seismic motion, *J. Geophys. Res.* **101**, 5835–5846.
- Campillo, M. and M. Bouchon (1985). Synthetic SH seismograms in laterally varying medium by discrete wavenumber method, *Geophys. J. R. Astr. Soc.* **83**, 307–317.
- Canuto, C. and D. Funaro (1988). The Schwarz algorithm for spectral methods, *SIAM J. Numer. Anal.* **25**, 24–40.
- Carcione, J. M. (1991). Domain decomposition for wave propagation problems, *J. Sci. Comp.* **6**, 453–472.
- Carcione, J. M. and P. J. Wang (1993). A Chebyshev collocation method for the wave equation in generalized coordinates, *Comp. Fluid Dyn. J.* **2**, 269–290.
- Carver, D. L., K. W. King, E. Cranswick, D. W. Worley, P. Spudich, and C. Mueller (1990). Digital recordings of aftershocks of the October 17, 1989, Loma Prieta, California, earthquake: Santa Cruz, Los Gatos, and surrounding areas, *U.S. Geol. Surv. Open-File Rept.* 90–683, 204 pp.
- Clayton, R. and B. Engquist (1977). Absorbing boundary conditions for acoustic and elastic wave equations, *Bull. Seism. Soc. Am.* **67**, 1529–1540.
- Clouser, R. H. and C. A. Langston (1995). Modeling observed  $P$ - $R_g$  conversions from isolated topographic features near the NORESS array, *Bull. Seism. Soc. Am.* **85**, 859–873.
- Dablain, M. A. (1986). The application of high-order differencing to the scalar wave equation, *Geophysics* **51**, 54–66.
- de Bremaecker, J. C. (1958). Transmission and reflection of Rayleigh waves at corners, *Geophysics* **23**, 253–266.
- de Hoop, A. T. (1960). A modification of Cagniard's method for solving seismic pulse problems, *Appl. Sci. Res.* **B8**, 349–356.
- Dravinski, M. and T. K. Mossessian (1987). Scattering of plane harmonic  $P$ ,  $SV$  and Rayleigh waves by dipping layers of arbitrary shape, *Bull. Seism. Soc. Am.* **77**, 212–235.
- Engquist, B. and A. Majda (1977). Absorbing boundary conditions for the numerical simulation of waves, *Math. Comp.* **31**, 629–651.
- Faccioli, E., F. Maggio, A. Quarteroni, and A. Tagliani (1996). Spectral-domain decomposition methods for the solution of acoustic and elastic wave equations, *Geophysics* **61**, 1160–1174.
- Fisher, P. (1989). Spectral element solution of the Navier-Stokes equations on high performance distributed-memory parallel processors, *Ph.D. Thesis*, Massachusetts Institute of Technology, Cambridge, Massachusetts.
- Fisher, P. (1990). Analysis and application of a parallel spectral element method for the solution of the Navier-Stokes equations, *Comp. Meth. Appl. Mech. Eng.* **80**, 483–491.
- Fornberg, B. (1988). The pseudospectral method: accurate representation of interfaces in elastic wave calculations, *Geophysics* **53**, 625–637.
- Frankel, A. (1993). Three-dimensional simulations of ground motions in the San Bernardino valley, California, for hypothetical earthquakes on the San Andreas fault, *Bull. Seism. Soc. Am.* **83**, 1020–1041.
- Gaffet, S. and M. Bouchon (1989). Effects of two-dimensional topographies using the discrete wavenumber-boundary integral equation method in  $P$ - $SV$  cases, *J. Acoust. Soc. Am.* **85**, 2277–2283.
- Gao, S., H. Liu, P. M. Davis, and L. Knopoff (1996). Localized amplification of seismic waves and correlation with damage due to the Northridge earthquake: evidence for focusing in Santa Monica, *Bull. Seism. Soc. Am.* **86**, S209–S230.
- Garvin, W. W. (1956). Exact transient solution of the buried line source problem, *Proc. R. Soc. London Ser. A* **234**, 528–541.
- Gazdag, J. (1981). Modeling of the acoustic wave equation with transform methods, *Geophysics* **46**, 854–859.
- Gilbert, F. and L. Knopoff (1960). Seismic scattering from topographic irregularities, *J. Geophys. Res.* **65**, 3437–3444.
- Givoli, D. (1991). Non-reflecting boundary conditions: review article, *J. Comput. Phys.* **94**, 1–29.
- Givoli, D. and J. B. Keller (1990). Non-reflecting boundary conditions for elastic waves, *Wave Motion* **12**, 261–279.
- Gottlieb, D. (1981). The stability of pseudospectral Chebyshev methods, *Math. Comp.* **36**, 107–118.
- Horike, M., H. Uebayashi, and T. Takeuchi (1990). Seismic response in three dimensional sedimentary basin due to plane S wave incidence, *J. Phys. Earth* **38**, 261–284.
- Hudson, J. A. and L. Knopoff (1964). Transmission and reflection of surface waves at a corner, part 2: Rayleigh waves (theoretical), *J. Geophys. Res.* **69**, 281–289.
- Hughes, T. J. R. (1987). *The Finite Element Method, Linear Static and Dynamic Finite Element Analysis*, Prentice-Hall International, Englewood Cliffs, New Jersey.
- Hughes, T. J. R. and J. E. Marsden (1978). Classical elastodynamics as a linear symmetric hyperbolic system, *J. Elasticity* **8**, 97–110.
- Hulbert, G. M. and T. J. R. Hughes (1990). Space-time finite element methods for second-order hyperbolic equations, *Comp. Meth. Appl. Mech. Eng.* **84**, 327–348.
- Iwata, T., K. Hatayama, H. Kawase, and K. Irikura (1996). Site amplification of ground motions during aftershocks of the 1995 Hyogo-ken Nanbu earthquake in severely damaged zone, *J. Phys. Earth* **44**, 563–576.
- Jih, R. S., K. L. McLaughlin, and Z. A. Der (1988). Free-boundary conditions of arbitrary polygonal topography in a two-dimensional explicit elastic finite-difference scheme, *Geophysics* **53**, 1045–1055.
- Kawase, H. and K. Aki (1989). A study on the response of a soft sedimentary basin for incident  $S$ ,  $P$  and Rayleigh waves, with special reference to the long duration observed in Mexico City, *Bull. Seism. Soc. Am.* **79**, 1361–1382.
- Kelly, K. R., R. W. Ward, S. Treitel, and R. M. Alford (1976). Synthetic seismograms: a finite difference approach, *Geophysics* **41**, 2–27.
- Khun, M. J. (1985). A numerical study of Lamb's problem, *Geophys. Prosp.* **33**, 1103–1137.
- Kim, J. and A. Papageorgiou (1993). Discrete wavenumber boundary element method for 3D scattering problems, *J. Eng. Mech. ASCE* **119**, 603–624.
- Komatitsch, D. (1997). Méthodes spectrales et éléments spectraux pour l'équation de l'élastodynamique 2D et 3D en milieu hétérogène, *Ph.D. Thesis*, Institut de Physique du Globe de Paris, Paris.
- Komatitsch, D., F. Couetel, and P. Mora (1996). Tensorial formulation of the wave equation for modelling curved interfaces, *Geophys. J. Int.* **127**, 156–168.
- Komatitsch, D., J. P. Vilotte, R. Vai, and F. J. Sánchez-Sesma (1998). The

- Spectral Element method for elastic wave equations: application to 2D and 3D seismic problems, *Int. J. Num. Meth. Eng.*, submitted.
- Kosloff, D. and E. Baysal (1982). Forward modeling by the Fourier method, *Geophysics* **47**, 1402–1412.
- Kosloff, D. and H. Tal-Ezer (1993). A modified Chebyshev pseudospectral method with an  $O(N^{-1})$  time step restriction, *J. Comput. Phys.* **104**, 457–469.
- Kosloff, D., D. Kessler, A. Q. Filho, E. Tessmer, A. Behle, and R. Strahl- evitz (1990). Solution of the equations of dynamics elasticity by a Chebyshev spectral method, *Geophysics* **55**, 748–754.
- Lamb, H. (1904). On the propagation of tremors over the surface of an elastic solid, *Phil. Trans. R. Soc. London. Ser. A* **203**, 1–42.
- Lapwood, E. R. (1961). The transmission of a Rayleigh pulse round a corner, *Geophys. J.* **4**, 174–196.
- Levander, A. R. (1988). Fourth-order finite-difference *P-SV* seismograms, *Geophysics* **53**, 1425–1436.
- Lysmer, J. and L. A. Drake (1972). A finite element method for seismology, in *Methods in Computational Physics*, Vol. 11, Academic, New York.
- Lysmer, J. and R. L. Kuhlemeyer (1969). Finite dynamic model for infinite media, *J. Eng. Mech. Div. ASCE 95 EM 4*, 859–877.
- Madariaga, R. (1976). Dynamics of an expanding circular fault, *Bull. Seism. Soc. Am.* **65**, 163–182.
- Maday, Y. and A. T. Patera (1989). Spectral element methods for the incompressible Navier-Stokes equations, in *State of the Art Survey in Computational Mechanics*, A. K. Noor and J. T. Oden (Editors), ASME, New York, 71–143.
- Maday, Y. and A. Quarteroni (1982). Approximation of Burgers equation by pseudospectral methods, *RAIRO Anal. Numer.* **16**, 375–404.
- Maday, Y. and E. M. Rønquist (1990). Optimal error analysis of spectral methods with emphasis on non-constant coefficients and deformed geometries, *Comp. Meth. Appl. Mech. Eng.* **80**, 91–115.
- Manolis, G. and D. E. Beskos (1988). *Boundary Element Methods in Elastodynamics*, Umwin Hyman, London.
- Marfurt, K. J. (1984). Accuracy of finite-difference and finite-element modeling of the scalar wave equations, *Geophysics* **49**, 533–549.
- Ohminato, T. and B. A. Chouet (1997). A free-surface boundary condition for including 3D topography in the finite difference method, *Bull. Seism. Soc. Am.* **87**, 494–515.
- Ohuri, M., K. Koketsu, and T. Minomi (1992). Seismic response of three dimensional sediment filled valleys due to incident plane waves, *J. Phys. Earthquake* **40**, 209–222.
- Olsen, K. B. and R. J. Archuleta (1996). 3-D simulation of earthquakes on the Los Angeles fault system, *Bull. Seism. Soc. Am.* **86**, 575–596.
- Orszag, S. A. (1980). Spectral methods for problems in complex geometries, *J. Comput. Phys.* **37**, 70–92.
- Patera, A. T. (1984). A spectral element method for fluid dynamics: laminar flow in a channel expansion, *J. Comput. Phys.* **54**, 468–488.
- Pedersen, H. A., B. LeBrun, D. Hatzfeld, M. Campillo, and P. Bard (1994). Ground motion amplitude across ridges, *Bull. Seism. Soc. Am.* **84**, 1786–1800.
- Pilant, W. L. (1979). *Elastic Waves in the Earth*, Elsevier, Amsterdam.
- Pitarka, A. and K. Irikura (1996). Basin structure effects on long period strong motions in the San Fernando valley and the Los Angeles basin from the 1994 Northridge earthquake and aftershocks, *Bull. Seism. Soc. Am.* **86**, S126–S137.
- Priolo, E., J. M. Carcione, and G. Seriani (1994). Numerical simulation of interface waves by high-order spectral modeling techniques, *J. Acoust. Soc. Am.* **95**, 681–693.
- Richter, G. R. (1994). An explicit finite element method for the wave equation, *Appl. Num. Math.* **16**, 65–80.
- Robertsson, J. O. A. (1996). A numerical free-surface condition for elastic/viscoelastic finite-difference modeling in the presence of topography, *Geophysics* **61**, 1921–1934.
- Rulf, B. (1969). Rayleigh waves on curved surfaces, *J. Acoust. Soc. Am.* **45**, 493–499.
- Sánchez-Sesma, F. J. (1983). Diffraction of elastic waves by three-dimensional surface irregularities, *Bull. Seism. Soc. Am.* **73**, 1621–1636.
- Sánchez-Sesma, F. J. (1997). Strong ground motion and site effects, in *Computer Analysis and Design of Earthquake Resistant Structures*, D. Beskos and S. Angnostopoulos (Editors), Comp. Mech. Publications, Southampton, 201–239.
- Sánchez-Sesma, F. J. and M. Campillo (1993). Topographic effects for incident *P*, *SV* and Rayleigh waves, *Tectonophysics* **218**, 113–125.
- Sánchez-Sesma, F. J. and F. Luzón (1996). Can horizontal *P* waves be trapped and resonate in a shallow sedimentary basin? *Geophys. J. Int.* **124**, 209–214.
- Sánchez-Sesma, F. J. and E. Rosenblueth (1979). Ground motion at canyons of arbitrary shape under incident *SH* waves, *Int. J. Earthquake Eng. Struct. Dyn.* **7**, 441–450.
- Simo, J. C., N. Tarnow, and K. K. Wong (1992). Exact energy-momentum conserving algorithms and symplectic schemes for nonlinear dynamics, *Comp. Meth. Appl. Mech. Eng.* **100**, 63–116.
- Spudich, P., M. Hellweg, and W. H. K. Lee (1996). Directional topographic site response at Tarzana observed in aftershocks of the 1994 Northridge, California, earthquake: implications for mainshock motions, *Bull. Seism. Soc. Am.* **86**, S193–S208.
- Stacey, R. (1988). Improved transparent boundary formulations for the elastic wave equation, *Bull. Seism. Soc. Am.* **78**, 2089–2097.
- Szabó, B. and I. Babuška (1991). *Finite Element Analysis*, Wiley, New York.
- Tessmer, E., D. Kosloff, and A. Behle (1992). Elastic wave propagation simulation in the presence of surface topography, *Geophys. J. Int.* **108**, 621–632.
- Toki, K., K. Irikura, and T. Kagawa (1995). Strong motion records in the source area of the Hyogo-ken Nanbu earthquake, January 17, 1995, *J. Nat. Disast. Sci.* **16**, 23–30.
- Tordjman, N. (1995). Éléments finis d'ordre élevé avec condensation de masse pour l'équation des ondes, *Ph.D. Thesis*, Université Paris IX Dauphine, Paris.
- Toshinawa, T. and T. Ohmachi (1992). Love wave propagation in three-dimensional sedimentary basin, *Bull. Seism. Soc. Am.* **82**, 1661–1667.
- Umeda, Y., A. Kuroiso, K. Ito, Y. Ito, and T. Saeki (1986). High accelerations in the epicentral area of the western Nagana prefecture, Japan, earthquake of 1984, *J. Seism. Soc. Jpn.* **39**, 217–228.
- Virieux, J. (1986). *P-SV* wave propagation in heterogeneous media: velocity-stress finite-difference method, *Geophysics* **51**, 889–901.
- Zhang, L. and A. K. Chopra (1991). Three-dimensional analysis of spatially varying ground motions around a uniform canyon in a homogeneous half-space, *Int. J. Earthquake Eng. Struct. Dyn.* **20**, 911–926.

## Appendix A

The semi-discrete variational form of the momentum equation, corresponding to equation (13), can be given by

$$\begin{aligned}
 \mathbf{A} \sum_{e=1}^{nel} \left[ \int_{\Omega_e} \rho \dot{\mathbf{v}}_N^h \cdot \mathbf{w}_N^h dV + \int_{\Omega_e} \nabla \mathbf{w}_N^h : \mathbf{c} : \nabla \mathbf{u}_N^h dV \right] \\
 = \mathbf{A} \sum_{e=1}^{nel} \left[ \int_{\Omega_e} \mathbf{f} \cdot \mathbf{w}_N^h dV \right. \\
 + \int_{\Gamma_{int}^e} \mathbf{T} \cdot \mathbf{w}_N^h d\Gamma \\
 \left. + \int_{\Gamma_{ext}^e} \mathbf{t} \cdot \mathbf{w}_N^h d\Gamma \right], \quad (\text{A1})
 \end{aligned}$$

where  $\mathbf{A}$  is the standard assembly operator over the total number of spectral elements, and  $\mathbf{u}_N^h \in \mathcal{S}_N^h$  and  $\mathbf{w}_N^h \in \mathcal{V}_N^h$ .

All the mathematical integrations involved at the element level are approximated by numerical ones. With the help of the local geometrical mapping  $\mathcal{F}_e$ , each integral is pulled back from the global coordinate system  $\mathbf{x}$  to the local coordinate system  $\xi$ . On each parent domain, the integral is evaluated using the Gauss–Lobatto Legendre quadrature:

$$\int_{\Omega_e} \nabla \mathbf{w}_N^h : \mathbf{c} : \nabla \mathbf{u}_N^h dV = \sum_{i,j,k} \tilde{\nabla} \mathbf{w}_N^h |_{\Omega_e}(\xi_i, \eta_j, \zeta_k) : \mathbf{c}(\xi_i, \eta_j, \zeta_k) : \tilde{\nabla} \mathbf{u}_N^h |_{\Omega_e}(\xi_i, \eta_j, \zeta_k) \omega_{ijk}, \quad (\text{A2})$$

$$\int_{\Omega_e} \mathbf{f} \cdot \mathbf{w}_N^h dV = \sum_{i,j,k} \mathbf{f} |_{\Omega_e}(\xi_i, \eta_j, \zeta_k) \cdot \mathbf{w}_N^h |_{\Omega_e}(\xi_i, \eta_j, \zeta_k) \omega_{ijk}, \quad (\text{A3})$$

where  $\Xi_N^e = \{(\xi_i, \eta_j, \zeta_k); 0 \leq i \leq N; 0 \leq j \leq N; 0 \leq k \leq N\}$  denotes the integration grid of  $(N+1)^3$  points within the reference domain;  $\omega_{ijk} = \omega_i \omega_j \omega_k$  with  $\omega_l > 0$  denotes the 1D Gauss–Legendre Lobatto quadrature weights, and  $\tilde{\nabla}$  denotes the pull back of the gradient operator in the  $\xi$  coordinate system:

$$\nabla_{\mathbf{x}} \mathbf{w}_N^h |_{\Omega_e} = \tilde{\nabla} \mathbf{w}_N^h |_{\Omega_e}(\xi) = \nabla_{\xi} \mathbf{w}_N^h |_{\Omega_e}(\xi) \mathbf{F}_e^{-1}(\xi), \quad (\text{A4})$$

where  $\mathbf{F}_e(\xi) = \partial_{\xi} \mathcal{F}_e(\xi)$  is the gradient of the local geometrical transformation. With the help of the Lagrangian interpolation, this leads to the system of ordinary differential equations (23), where now

$$\mathbf{M} = \mathbf{A} \int_{\Omega_e} (l^N \otimes l^N \otimes l^N) \otimes (l^N \otimes l^N \otimes l^N) \rho dV, \quad (\text{A5})$$

$$\mathbf{F}^{\text{int}} = \mathbf{A} \left[ \int_{\Omega_e} \nabla (l^N \otimes l^N \otimes l^N) : \mathbf{c} : \nabla \mathbf{u}_N^h |_{\Omega_e} dV - \int_{\Gamma^{\text{ext}}_e} (l^N \otimes l^N \otimes l^N) \mathbf{t}(\mathbf{v}_N^h) d\Gamma \right], \quad (\text{A6})$$

$$\mathbf{F}^{\text{ext}} = \mathbf{A} \left[ \int_{\Omega_e} (l^N \otimes l^N \otimes l^N) \mathbf{f} dV + \int_{\Gamma^{\text{int}}_e} (l^N \otimes l^N \otimes l^N) \mathbf{T} d\Gamma \right]. \quad (\text{A7})$$

For a seismic source described in terms of a distribution of moment-tensor density  $\mathbf{f}(\mathbf{x}, t) = -\text{div}[\mathbf{m}(\mathbf{x}, t)]$ , with a localized spatial support, the generalized body force can be written after integration by part as

$$\mathbf{A} \int_{\Omega_e} \nabla (l^N \otimes l^N \otimes l^N) : \mathbf{m}(\mathbf{x}, t) dV, \quad (\text{A7})$$

where the assembly operation involves all the elements that

belong to the definition of the spatial support of the moment density distribution.

In contrast with classical finite-element methods, the mass matrix is diagonal by construction, leading to fully explicit time schemes. Heterogeneities can be handled naturally in two different ways: either by prescribing different material properties for each spectral element or by assigning different properties at each collocation point, allowing, therefore, for the description of highly variable velocity structures.

## Appendix B

The semi-discrete momentum equation is enforced in conservative form at  $t_{n+a}$ . This energy-momentum conserving scheme can be generalized to a predictor–multi-corrector format that improves its characteristics under some circumstances, and it allows for an efficient parallel implementation. The implementation sequence is as follows:

$$i = 0 \quad (i \text{ is the iteration number})$$

Predictor phase:

$$\mathbf{d}_{n+1}^{(i)} = \tilde{\mathbf{d}}_{n+1} \quad \mathbf{v}_{n+1}^{(i)} = 0 \quad \mathbf{a}_{n+1}^{(i)} = \tilde{\mathbf{a}}_{n+1}.$$

Solution phase:

$$\frac{1}{\Delta t} \mathbf{M} \Delta \mathbf{v}^{(i)} = \mathbf{F}_{n+a}^{\text{ext}} - \mathbf{F}^{\text{int}}(\mathbf{d}_{n+a}^{(i)}, \mathbf{v}_{n+a}^{(i)}) - \frac{1}{\Delta t} \mathbf{M}(\mathbf{v}_{n+1}^{(i)} - \mathbf{v}_n).$$

Corrector phase:

$$\mathbf{v}_{n+1}^{(i+1)} = \mathbf{v}_{n+1}^{(i)} + \Delta \mathbf{v},$$

$$\mathbf{d}_{n+1}^{(i+1)} = \tilde{\mathbf{d}}_{n+1} + \frac{\beta \Delta t}{\gamma} \mathbf{v}_{n+1}^{(i+1)},$$

$$\mathbf{a}_{n+1}^{(i+1)} = \tilde{\mathbf{a}}_{n+1} - \frac{1}{\gamma \Delta t} \mathbf{v}_{n+1}^{(i+1)},$$

where the predictors are defined as

$$\tilde{\mathbf{d}}_{n+1} = \mathbf{d}_n + \Delta t \left( 1 - \frac{\beta}{\gamma} \right) \mathbf{v}_n + \Delta t^2 \left( \frac{1}{2} - \frac{\beta}{\gamma} \right) \mathbf{a}_n,$$

$$\tilde{\mathbf{a}}_{n+1} = \left( 1 - \frac{1}{\gamma} \right) \mathbf{a}_n - \frac{1}{\gamma \Delta t} \mathbf{v}_n,$$

with  $\mathbf{d}_{n+a} = \alpha \mathbf{d}_{n+1} + (1 - \alpha) \mathbf{d}_n$  and  $\mathbf{F}_{n+a}^{\text{ext}} = \alpha \mathbf{F}_{n+1}^{\text{ext}} + (1 - \alpha) \mathbf{F}_n^{\text{ext}}$ .

Exact conservation of the total angular momentum is achieved for the values  $\alpha = \beta/\gamma = 1/2$  corresponding to the

conservation form of the mid-point rule. These values define an acceleration-independent time-marching algorithm. Second-order accuracy is achieved if and only if  $\alpha = 1/2$ . For the parameter values  $\alpha = \beta/\gamma = 1/2$ , a linear analysis shows that the spurious root at zero sampling frequency vanishes if and only if  $\gamma = 1$ . This value yields the post-processing formula  $\mathbf{a}_{n+1} = (\mathbf{v}_{n+1} - \mathbf{v}_n)/\Delta t$ . Within this energy-momentum conserving framework, there is no difficulty to

handle a more complex constitutive behavior, in particular to incorporate attenuation.

Département de Sismologie (URA 195)  
Institut de Physique du Globe de Paris  
4, Place Jussieu  
75252—Paris Cedex 05, France

Manuscript received 17 July 1997.